University of Alberta

KELVIN-HELMHOLTZ INSTABILITY OF A BOTTOM-INTENSIFIED JET

by

Chandana R. Somayaji

A thesis submitted to the Faculty of Graduate Studies and Research
in partial fulfillment of the requirements for the degree of

Master of Science

in

Applied Mathematics

Department of Mathematical and Statistical Sciences

Fall 2013

Edmonton, Alberta

Abstract

The Kelvin-Helmholtz instability is the inertial destabilization of a parallel shear flow in a density stratified fluid under the influence of gravity. For example, this type of instability manifests itself as surface waves in the ocean when wind blows over the water surface. In this thesis we solve the nonhydrostatic Kelvin-Helmholtz instability problem for a near-bottom jet with a continuous velocity profile in a flat-bottomed non-rotating density-stratified fluid. Of particular note, the nonhydrostatic stability problem modelled here has a high wavenumber cutoff and does not exhibit an ultraviolet catastrophe unlike other inviscid stability calculations that have been previously published.

Acknowledgements

First and foremost, a heartfelt thanks to my supervisor, Dr Gordon Swaters, for his persistent support, advice and words of encouragement throughout this project. His passionate attitude towards research and writing has helped me acquire a great appreciation of the same and I know I will be taking those things with me wherever I go. Thank you, Gordon!

Thanks also goes to Dr John Bowman and Dr Michael Li for their roles as committee members and for providing useful comments towards the betterment of the thesis.

My friends, who helped keep me (relatively) sane throughout my time at school, thank you very much!

There are no words to express my gratitude towards my family- parents and sister- for their immeasurable love, patience, guidance and friendship. This is dedicated to you.

Contents

List of Figures

Chapter 1

Introduction

1.1 Hydrodynamic Stability

The analysis of stability and the onset of instability (instability which sometimes develops into turbulence) comprises the study of hydrodynamic stability. The fundamental problems of hydrodynamic stability were first developed in the nineteenth century by Helmholtz, Kelvin, Rayleigh and Reynolds [6]. A series of experiments performed by Reynolds [20], the results of which were published in his paper in 1883, provided a clear introduction to the problems of stability. His experiments were an attempt to study the instability of a flow through a pipe. Later experiments introduced perturbations of finite amplitude using different flow profiles with the aim of finding whether a particular flow is unstable [6]. The theories and methods of hydrodynamic stability can be applied to a multitude of fields including, and not restricted to, magnetohydrodynamics, elasticity, plasma physics and general relativity. The physics in these areas are very different; however, the mathematics applied is similar in that nonlinear partial differential equations describing the physical model are examined by studying the stability of the known solutions of the equations [6]. One can study the instabilities of flows and their transition to turbulence by a few methods such as performing physical and numerical experiments, observing natural phenomena, applying linear, weakly nonlinear theory or strongly

nonlinear theory and also, by applying the theories of bifurcation and chaos.

One area of study that the theories of hydrodynamic stability can be applied to is physical oceanography. Abyssal currents play a significant role in ocean circulation. In this context, Swaters [22] investigated the stability characteristics of overflows that were non rotating and baroclinic, and where it was possible for both frictionally induced and Kelvin-Helmholtz instability to occur. A two-layered shallow-water model was used, resulting in the Kelvin-Helmholtz instability being hydrostatic. In the inviscid limit, the linear stability analysis of the two-layered shallow-water equations lead to an ultraviolet catastrophe [16]. Since this is not a desirable part of the model, in this thesis, we attempt a step toward gaining a better understanding of the instability in the nonhydrostatic case, where, in most cases, the most unstable mode is located at a finite wavenumber and there exists a high wavenumber cutoff. The work done in this thesis is based on the application of the linear stability theory to the given flow profile.

1.2 Linear stability theory and the method of normal modes

In linear stability theory (LST), we first consider a basic flow profile that might be of interest, and which is a known solution to the fully nonlinear equations of motion that govern the flow. The perturbations quantifying the velocity and pressure fields, which are generally considered infinitesimally small, are then introduced. In essence, a given flow is said to be stable if all perturbations which are initially small will remain so for all time and the flow is unstable if even a single perturbation that starts off as initially small grows to such an extent it can no longer be neglected. The linear stability of the flow is then investigated by neglecting products of the perturbed quantities in the equations of motion and the boundary conditions, which gives us the linearized problem [6]. This method of studying the stability of systems was originally used

for studying the oscillations and instability of dynamical systems of particles and rigid bodies, in which case, known solutions of Newton's or Lagrange's equations of motion were perturbed and nonlinear terms in the perturbation fields were neglected [6]. The method was later adapted by Stokes, Kelvin and Rayleigh to fluid dynamics, the main mathematical difference being that the equations of motion are partial, rather than ordinary differential equations.

Each perturbation is further resolved into independent components or modes that vary in time t like e^{ct}, where c is a constant which is generally complex. The values of c are then calculated for the linearized problem. If the real part of c is positive, the system is said to be unstable since the initial disturbance grows exponentially in time. If no such unstable state can be found, the system is stable. This method of analysis involving the examination of the Fourier components is called the *normal mode method* [15]. In this method, the stability of each method is examined separately, since the linearity of the problem implies that the various modes do not interact. This leads to an eigenvalue problem, as we will see.

LST has a few advantages. It provides a fairly satisfactory description of the solutions of most initial value problems starting near the basic state, provided one does not follow the solution for a long time. Problems that are otherwise accessible only by numerical computations can be solved analytically when linear stability theory is properly supplemented with appropriate approximations especially near special regions like boundaries and critical layers [13]. On the other hand, one of the main disadvantages of LST is the poor approximation made if the initially small disturbances become larger at a later time. In such cases, it is a more viable option to consider either weakly nonlinear or strongly nonlinear disturbances in getting more accurate conditions for stability. We will be applying this theory to study Kelvin-Helmoltz instability exhibited by the flow profile considered.

1.3 Kelvin-Helmholtz instability

Kelvin-Helmholtz (K-H) instability is the instability of a parallel shear flow in a density stratified fluid under the influence of gravity, and is a mechanism for many phenomena observed in the ocean and atmosphere. Kelvin formulated and solved a prototypical problem of linear instability of a basic flow of incompressible inviscid fluids in two horizontal parallel infinite streams of different densities and velocities, with one stream over the other [7]. The model was initially applied in the investigation of ocean-wave generation by the wind. Helmholtz developed the same model to apply it to billow clouds. It is also one of the main instability mechanisms for high Reynolds number, near parallel flows, such as jets [6]. The instability forms as a series of vortices that have a structure of rolling billows and are periodic. The two-dimensional evolution of these billows is followed by the growth of three-dimensional secondary instabilities, which then transition to turbulence.

K-H instabilities can be studied using different methods. Theoretically, the onset of K-H waves and their initial stages of growth can be described by linear stability analysis. The waves can also be generated in laboratories, which allows for detailed examination of the evolution of the billows through their entire life cycle (see for example, [4]). Numerical simulations provide a tool for accurate quantifications of K-H flow fields, albeit under idealized conditions (eg., [10]). All of these approaches are meant to complement one another to provide a better understanding of the instabilities.

Typically, a background shear flow of $U_0(z)$, background pressure $p_H(z)$, and vertical density stratification, $\rho_H(z)$ are considered. The background pressure is assumed to be in hydrostatic balance in the absence of any motion ($u = 0$). Another assumption made in using the two-dimensional model equations is based on Squire's theorem ([16]), which states that: "For each unstable three-dimensional wave there is always a more unstable two-dimensional one traveling parallel to the flow". This flow is perturbed with a small two dimensional perturbation velocity of the form (u', w') and pressure p' to give the

total velocity field (u, w) and pressure p,

$$u = U_0(z) + u'(x, z, t),$$

$$w = 0 + w'(x, z, t),$$

$$p = p_H(z) + p'(x, z, t),$$

and

$$\rho = \rho_H(z) + \rho'(x, z, t).$$

where p_H and ρ_H are the background hydrostatic pressure and hydrostatic density, respectively. For this two dimensional flow, we can write the Navier-Stokes equations in terms of the conservation of horizontal and vertical momentum,

$$\rho\left(\frac{\partial u}{\partial t} + u\frac{\partial u}{\partial x} + w\frac{\partial u}{\partial z}\right) = -\frac{\partial p}{\partial x},$$

$$\rho\left(\frac{\partial w}{\partial t} + u\frac{\partial w}{\partial x} + w\frac{\partial w}{\partial z}\right) = -\frac{\partial p}{\partial z} - \rho g,$$

the incompressibility equation,

$$\frac{\partial \rho}{\partial t} + u\frac{\partial \rho}{\partial x} + w\frac{\partial \rho}{\partial z} = 0,$$

and the continuity equation,

$$u_x + w_z = 0.$$

The stability of the background flow to the perturbations is linearly analyzed by substituting the linearization equations into the Navier-Stokes equations and neglecting the terms that have products of perturbations. The resulting linear equations are solved conventionally by using the method of normal modes. A perturbation quantity, ϕ, is assumed of the form

$$\phi(x, z, t) = \tilde{\phi}(z)e^{ik(x-ct)} + \text{c.c.},$$

where $i^2 = -1$, k is the horizontal direction wave number of the mode, c is the complex phase speed, and c.c. denotes the complex conjugate of the preceding term. Substituting these in the linear equations of motion, we get a nonstandard eigenvalue problem that has c as the "eigenvalue" and $\tilde{\phi}$ as the eigenfunction. For each mode, $c = c_R + ic_I$ and kc_I is the exponential growth rate of the mode. The stability characteristics of the flow profile can be investigated from the dispersion relation obtained by solving an eigenvalue problem.

The model that Kelvin developed was a first attempt at understanding the shear layer instability [7]. The instability occurs at the interface between the horizontal parallel streams, and is brought forth when the stabilizing influence of the stratification is overcome by the destabilizing influence of shear [15]. Stratified shear layer instability has been examined fairly extensively. Esch [8] considered a parallel flow of a shear layer between uniform streams to examine the stability of a piecewise linear velocity profile. His analysis also extended to include viscous effects. He changed the model slightly by completely neglecting the effects of viscosity in his 1961 paper [9]. Howard and Maslowe [13] gave a fairly comprehensive summary about the results of linear inviscid theory and also outlined the weakly non-linear and the non-linear theory.

1.4 Thesis outline

This thesis uses analytic linear theory to obtain the relevant stability characteristics for the flow profile studied. We first solve a simpler version of our main problem in Chapter 2, where we employ a three layered model in a fluid that is assumed to have no variations in density, i.e, one that is homogeneous, and a velocity that is piecewise continuous and linear. We will use the linearized equations of motion to first derive the Rayleigh Stability equation.

In order to reconcile the jump across the interface with the solutions of the model equations, the matching conditions are then derived. The kinematic matching condition says that a fluid parcel once on the boundary will remain on the boundary for all time, and the dynamic condition which states that the pressure field must be continuous across the moving boundary [7]. We will use these matching conditions along with the solutions of the model equations to determine the dispersion relation, which is quadratic in the phase velocity, c.

The marginal stability boundary is then obtained from the dispersion relation. The marginal stability boundary thus derived is dependent on the flow parameters k, h_0 and d, i.e., the wave number, the mean layer depth of the middle layer and the mean layer depth of the lower layer, respectively. Because of the complexity of the dispersion relation and to enable us to understand the stability characteristics better, we study the transition from stability to instability one parameter at a time. Lastly, we will examine the asymptotic structure of the dispersion relation to explain some of the singularities observed. We will see in this chapter that for typical values for a bottom intensified shear flow, we get a dimensional high and low wavenumber cutoff at 0.0077 m^{-1} and 0.0036 m^{-1}, respectively, which translates to a dimensional wavelength of about 815 m and 1.74 km, respectively. Using these values, the dimensional phase velocity, frequency, period of oscillation and growth rate of the most unstable mode are calculated. The e-folding amplification time corresponding to the growth rate of the most unstable mode is calculated to be 13.51 s.

In Chapter 3, we introduce a density variation for the same flow profile used in Chapter 2. A similar type of analysis is carried out, wherein we use the linearized equations of motion to first derive the Taylor-Goldstein equation. Having derived the matching conditions from the model equations, we use them along with the solutions of the model equations to determine the dispersion relation, which as it turns out, is cubic in this case. We then obtain the marginal stability boundary, which is dependent on the parameters, k, h_0, d, δ and F, where k, h_0 and d are the same as previously explained, and δ and F

are the stratification parameter and the Froude number, respectively.

The transition from stability to instability is again examined one parameter at a time. Finally, since the marginal stability boundary depends on δ, we will examine the effects of stratification on the stability of the flow. For typical values for a bottom intensified shear flow, the dimensional upper and lower wavenumber cutoffs are found to be 0.015 m^{-1} and 0.004 m^{-1}, respectively, which corresponds to a dimensional wavelength of about 418.88 m and 1.57 km, respectively. From these values, we can determine the dimensional phase velocity, frequency, period of oscillation and growth rate of the most unstable mode. The e-folding amplification in this case is calculated to be 27.3 s.

In chapter 4, we conclude with a summary of our results obtained and provide directions for any future work.

Chapter 2

Stability characteristics of a shear flow in a homogeneous fluid

The fundamental problem in the study of the stability of parallel flows is to determine whether a given shear flow is stable to traveling wave perturbations or not [16]. Since the work of Helmholtz [11] and Kelvin [14] on the stability of homogeneous and stratified vortex sheets in the 19th century, numerous authors have examined increasingly complex problems in an attempt to understand the basic properties associated with the transition to instability of fluid flows.

Rayleigh [18] examined a piecewise-linear representation of the homogeneous shear layer and performed a stability analysis on this idealized shear layer. The results produced are in qualitative agreement with subsequent studies of smooth profiles, such as the hyperbolic tangent shear layer (see, for example [5]). This suggests that in treating the stability of shear layers it is very useful to study piecewise linear shear layers in order to capture the basic instability mechanism ([3] [17]). Holmboe [12], motivated by geophysical flows, extended Rayleigh's analysis to include a stable density stratification, retaining the piecewise-linear shear layer and including a layered piecewise-constant

density profile. These idealized profiles give qualitatively similar results to the smooth profiles, as in the homogeneous case [10].

In the context of this thesis, we are interested in developing and analyzing simple models that can describe various aspects of the stability of deep, or abyssal, currents in the ocean. Our work is in the same spirit as the model developed by Swaters's [22] that describes the frictionally induced and Kelvin-Helmholtz instability in the context of non-rotating baroclinic abyssal overflows. The model was based on the two-layered shallow water equations and the resulting Kelvin-Helmholtz instability was hydrostatic. This does not enable one to investigate the nonhydrostatic shear layer Kelvin-Helmholtz instability. This work is a step toward gaining a better understanding of the shear layer instability in the nonhydrostatic case.

We start by introducing in this chapter a piecewise-linear homogeneous shear flow and studying in detail, the stability characteristics of the same. In Chapter 3, we include a stable density stratification to the piecewise-linear flow profile. In Section 2.1, the equations that govern the flow are introduced. In order to solve the linearized equations of motion and to reconcile the jump across the interface with the solutions of the model equations, we derive the matching conditions, as described in Section 2.2. In Section 2.3 we derive the dispersion relation from the solutions obtained. Sections 2.4-2.7 we discuss the stability characteristics from the dispersion relation.

2.1 Governing equations

We consider a three-layered flow profile that has a piecewise continuous and linear velocity with no variations in density, i.e., one that is homogeneous. The geometry of the three-layered model we are considering is shown in Fig. 2.1. The depth of the entire water column is H, η_1 and η_2 are the nondimensional disturbances in the middle and lower layer thicknesses, respectively, compared to the scale thickness and h_0 and d are the mean layer depths for the middle and lower layers, respectively.

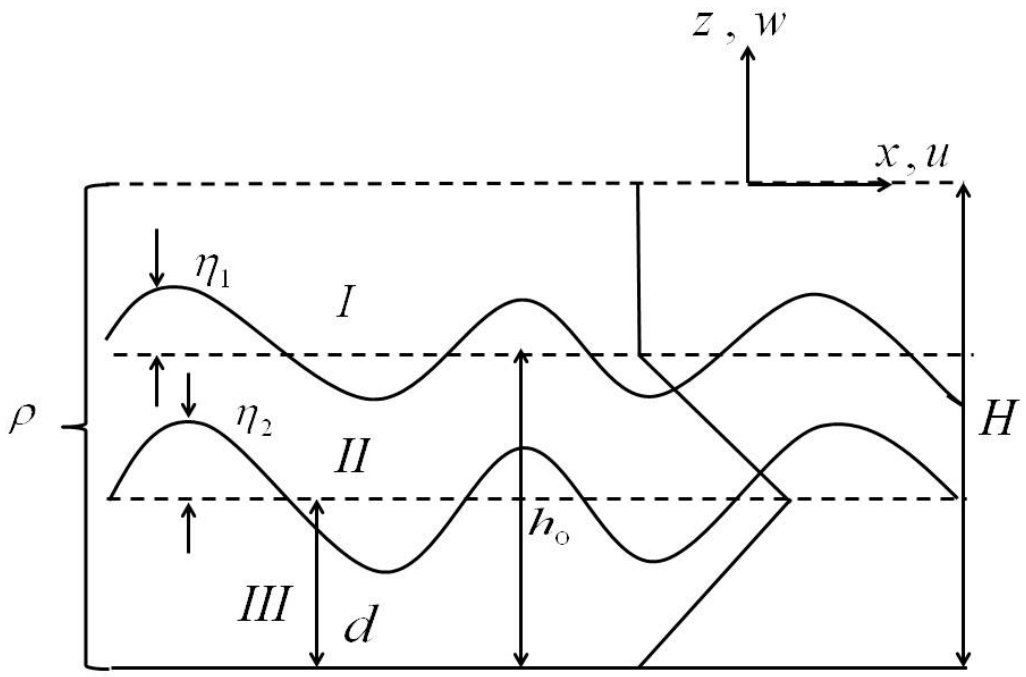

Figure 2.1: The geometry of the model.

The homogeneous, inviscid, incompressible 2-D flow is governed by the set of partial differential equations [15]:

$$\rho(\partial_t + u\partial_x + w\partial_z)u + p_x = 0, \tag{2.1}$$

$$\rho(\partial_t + u\partial_x + w\partial_z)w + p_z = -\rho g, \tag{2.2}$$

$$u_x + w_z = 0, \tag{2.3}$$

where u, w are the velocities in the positive x and z directions, respectively, ρ is the density which is constant throughout the layers, p is the total pressure field, g is the acceleration due to gravity and t is the time. Equations (2.1) and (2.2) represent the conservation of horizontal and vertical momentum, respectively,

and equation (2.3) express the conservation of mass. The quantities η_1 and η_2 depicted in Fig. 2.1 are the perturbation deflections of the interfaces located at $z = h_0$ and d, respectively.

In the absence of any motion, the fluid is assumed to be in hydrostatic balance. The hydrostatic rest state is given by (2.1), (2.2) and (2.3) where $u = w = 0$, with (2.2) reducing to

$$p_z = -\rho g, \tag{2.4}$$

which determines the background hydrostatic pressure given by

$$p_H(z) = -\rho g(z - H), \tag{2.5}$$

where we have imposed the boundary condition $p_H(H) = 0$.

One can show that $u = U_0(z), w = 0$ and $p = p_H(z)$ is an exact steady state solution of the equations of motion for any smooth function $U_0(z)$. From the x-direction momentum equation, (2.1),

$$\rho(\partial_t + U_0(z)\partial_x + 0\partial_z)U_0(z) + 0 = 0,$$

which gives

$$\rho \times 0 + 0 = 0.$$

Substituting the exact solution into the z-direction momentum equation, (2.2), we get

$$\rho(\partial_t + U_0(z)\partial_x + w\partial_z)0 + [p_H(z)]_z = \rho g,$$

which gives,

$$\frac{\partial p_H}{\partial z} = -\rho g,$$

which is satisfied on account of equation (2.5). The mass conservation equation with the exact solutions gives,

$$[U_0]_x + 0 = 0.$$

Since U_0 is a function of z alone, the above equation is trivially satisfied. We can thus conclude that $u = U_0(z), w = 0$ and $p = p_H(z)$ is an exact solution of the governing equations of motion.

We try to examine the linear stability of this exact solution. Thus, we now add perturbations to the exact solutions of the form,

$$u(x, z, t) = U_0(z) + \tilde{u}(x, z, t), \tag{2.6}$$

$$w(x, z, t) = \tilde{w}(x, z, t), \tag{2.7}$$

$$p(x, z, t) = p_H(z) + \tilde{p}(x, z, t), \tag{2.8}$$

where the tildes represent perturbation quantities. Substituting equations (2.6), (2.7) and (2.8) into our model equations (2.1), (2.2) and (2.3), neglecting nonlinear perturbation terms and dropping the tildes on the perturbation quantities, we get

$$\rho(\partial_t + U_0(z)\partial_x)u + \rho w U_0' = -p_x, \tag{2.9}$$

$$\rho(\partial_t + U_0(z)\partial_x)w = -p_z, \tag{2.10}$$

$$u_x + w_z = 0, \tag{2.11}$$

where equations (2.9), (2.10) and (2.11) are called the Linear Stability Equations and $U_0' \equiv \frac{dU_0(z)}{dz}$. Equations (2.9) and (2.10) are the perturbation momentum equations in the x and z direction respectively, and (2.11) is the perturbation continuity equation.

We now form the vorticity equation from $(2.10)_x - (2.9)_z$, i.e.,

$$[u_{zt} + U_0'(z)u_x + U_0(z)u_{xz} + w_z U_0'(z) + wU_0''(z) - w_{xt} - U_0(z)w_{xx}] = 0,$$

which simplifies to

$$(\partial_t + U_0\partial_x)(u_z - w_x) + (u_x + w_z)U_0' + U_0''w = 0.$$

It should be noted that in forming the vorticity equation, we have made use of the fact that p is twice differentiable. Since $u_x + w_z = 0$ is the continuity equation, (2.11), the vorticity equation reduces to

$$[\partial_t + U_0(z)\partial_x]\,(u_z - w_x) + wU_0''(z) = 0.$$

From the continuity equation, (2.11), it follows that there exists a stream-function $\phi(x, z, t)$ such that $u = -\phi_z$ and $w = \phi_x$ [7]. So, the above vorticity equation can be written in the form

$$(\partial_t + U_0\partial_x)\Delta\phi - U_0''\phi_x = 0, \tag{2.12}$$

where Δ is the 2D Laplacian operator defined by $\partial_{xx} + \partial_{zz}$.

The method of normal modes is used in Linear Stability Analysis whereby we introduce sinusoidal disturbances on a background steady state [15]. In our case, we superpose a disturbance on the background flow of the form,

$$\phi = \varphi(z)\exp[ik(x - ct)] + \text{c.c.},$$

where c.c is the complex conjugate of the preceding term. Here, $\varphi(z)$ corresponds to the amplitude function of the mode and is required to handle the vertical boundary conditions. The exponential part describes a wave propagating in the x-direction and k is the real-valued x-direction wavenumber (the wavelength is $\frac{2\pi}{k}$). The phase velocity, $c = c_R + ic_I$ is considered to be com-

plex, so instability occurs when $kc_I > 0$. Substituting the normal mode into equation (2.12), we get

$$-c\varphi''(z) + ck^2\varphi(z) + U_0\varphi''(z) - U_0k^2\varphi - U_0''\varphi = 0,$$

which simplifies to

$$(U_0 - c)\left[\varphi''(z) - k^2\varphi(z)\right] - U_0''\varphi = 0. \tag{2.13}$$

Equation (2.13) is the Rayleigh stability equation (henceforth, RSE) [7].

We take the background flow to be the piecewise continuous and linear, and given by,

$$U(z) = \begin{cases} 0 & h_0 \le z \le H, \\ \frac{U_0(z-h_0)}{d-h_0} & d \le z \le h_0, \\ \frac{U_0 z}{d} & 0 \le z \le d. \end{cases}$$

This profile is a model for a boundary jet located immediately adjacent to the bottom where the velocity is continuous but not differentiable and the maximum velocity is located at $z = d$ and the minimum jet velocity ($U_0(z) = 0$) is located at $z = h_0$ in the flow interior. As shown in Fig. 2.1, the interval $h_0 < z < H$ will be defined as region I, $d < z < h_0$ will be defined as region II and $0 < z < d$ will be defined as region III.

Since the flow profile is linear (i.e., $U_0'' \equiv 0$, except at the interfaces), the RSE reduces to

$$\varphi'' - k^2\varphi = 0,$$

in all three regions.

We will solve the RSE in each region and then match the solutions across the interfaces where U_0' and U_0'' are not defined, both at $z = h_0$ and $z = d$,

respectively, using appropriate jump conditions. The solutions for the three regions can be written in the form,

$$\varphi_I(z) = A\sinh[k(H-z)], \tag{2.14}$$

$$\varphi_{II}(z) = B\sinh[k(z-d)] + D\sinh[k(h_0-z))], \tag{2.15}$$

and,

$$\varphi_{III}(z) = E\sinh[kz], \tag{2.16}$$

where φ_I, φ_{II} and φ_{III}, are the solutions in layers I, II and III, respectively. The boundary conditions, $w = 0 \implies \phi_x = 0 \implies \varphi = 0$ at $z = H$ (a rigid lid) and at $z = 0$ (non-sloping bottom) are satisfied by (2.14) and (2.16), respectively. We note that in the solutions obtained above, A, B, D and E are as yet arbitrary constants.

2.2 Matching conditions

We now impose two matching conditions across each of the interfaces at $z = h_0$ and $z = d$. The first condition is the kinematic condition, which states that fluid particles on the interface must move with the interface without the two fluids occupying the same point at the same time and without a cavity forming between the fluids [16].

We first consider the interface located at $z = h_0$ and denote u^+, w^+ as $\lim_{z\to h_0^+} u, w$, and u^-, w^- as $\lim_{z\to h_0^-} u, w$. The fully nonlinear kinematic condition is given by [7],

$$w = \phi_x = \eta_{1t} + u\eta_{1x} \tag{2.17}$$

on $z = h_0 + \eta_1$, where η_1 is the perturbation to the location of the interface, which in the background flow is located at $z = h_0$. Substituting the perturbed solutions, (2.6), (2.7) and (2.8), into the nonlinear condition (2.17), Taylor

expanding about $z = h_0$ and linearizing, we get

$$w^+ = \eta_{1t} + U_0(h_0^+)\eta_{1x}, \tag{2.18}$$

at $z = h_0^+$, and

$$w^- = \eta_{1t} + U_0(h_0^-)\eta_{1x}, \tag{2.19}$$

at $z = h_0^-$.

It is now convenient to introduce normal modes of the form

$$w = \tilde{w}(z)\exp[ik(x - ct)] + \text{c.c.}, \tag{2.20}$$

$$\eta_1 = \eta_0 \exp[ik(x - ct)] + \text{c.c.}, \tag{2.21}$$

where η_0 is a complex constant. Substituting the normal modes, (2.20) and (2.21) into the linearized equations (2.18) and (2.19) and dropping the tildes, we get

$$w(h_0^+) = ik\eta_0[U_0(h_0^+) - c] \Rightarrow ik\eta_0 = \frac{w(h_0^+)}{U_0(h_0^-) - c},$$

and

$$w(h_0^-) = ik\eta_0[U_0(h_0^-) - c] \Rightarrow ik\eta_0 = \frac{w(h_0^-)}{U_0(h_0^-) - c},$$

which therefore implies

$$\frac{w(h_0^+)}{U_0(h_0^+) - c} = \frac{w(h_0^-)}{U_0(h_0^-) - c},$$

which can be rearranged in the form

$$\left[\frac{w}{U_0 - c}\right] = 0, \tag{2.22}$$

on $z = h_0$, where

$$[\star] \equiv \star^{+} - \star^{-}. \tag{2.23}$$

Equation (2.22) is a mathematical representation of the kinematic condition across the interface $z = h_0$. Since $w = ik\phi$ with the normal mode assumption and equation (2.17), the kinematic condition reduces to

$$\left[\frac{\phi}{U_0 - c}\right] = 0.$$

Finally, since $U_0(z)$ is continuous for all z , the kinematic condition reduces to

$$[\phi] = 0, \tag{2.24}$$

at $z = h_0$. Following a procedure similar to the one above, we get the same form for the kinematic condition, (2.24) at the $z = d$ interface.

The second matching condition we need is the dynamic condition which postulates that the normal component of the stress vector at the deforming interface is continuous [16]. Here again we first consider the condition across $z = h_0$ and then simply state what the appropriate condition should be across $z = d$.

For an inviscid fluid, stress continuity implies that the total pressure across the deforming interface is continuous [7], i.e,

$$p_{ITotal}(h_0 + \eta_1) = p_{IITotal}(h_0 + \eta_1), \tag{2.25}$$

where $p_{I,IITotal}$ are the total pressures in layers one and two, respectively, which are given by (2.7),

$$p_{ITotal} = p_H(z) + \tilde{p}_I(x, z, t), \tag{2.26}$$

and,

$$p_{IITotal} = p_H(z) + \tilde{p}_{II}(x, z, t), \tag{2.27}$$

where $\tilde{p}_I(x,z,t)$ and $\tilde{p}_{II}(x,z,t)$ are the perturbation pressures associated with the wave field in layers one and two, respectively. From (2.25), at $z = h_0 + \eta_1$,

$$p_H(h_0+\eta_1) + \tilde{p}_I(x, h_0+\eta_1, t) = p_H(h_0+\eta_1) + \tilde{p}_{II}(x, h_0+\eta_1, t),$$

which, if Taylor expanded about $z = h_0$ and linearized, reduces to

$$\tilde{p}_I(x, h_0, t) = \tilde{p}_{II}(x, h_0, t).$$

This gives the dynamic matching condition,

$$[p] = 0,$$

on $z = h_0$, where the tilde has been dropped.

We now introduce the normal mode assumptions,

$$p = \tilde{p}(z)\exp[ik(x-ct)] + c.c, \tag{2.28}$$

$$u = \tilde{u}\exp[ik(x-ct)] + c.c, \tag{2.29}$$

and

$$w = \tilde{w}\exp[ik(x-ct)] + c.c. \tag{2.30}$$

into the x-momentum equation, (2.9), and dropping the tildes, we find

$$\rho\left[ik(-c)u + ikU_0(z)u\right] - \rho U_0' w = -ikp. \tag{2.31}$$

Solving for p using $u = -\phi_z$ and $w = \phi_x$ gives

$$p = (U_0 - c)\phi' - U_0'\phi,$$

so that the dynamic matching condition across $z = h_0$ will be given by

$$[(U_0 - c)\phi' - U_0'\phi] = 0, \tag{2.32}$$

where the square brackets indicate the jump defined by (2.23). We get the same form for the condition for pressure continuity at the $z = d$ interface.

Now, applying the kinematic condition (2.24) at $z = h_0$ to the solutions (2.14) and (2.15) (i.e, $\phi_I(z)$ and $\phi_{II}(z)$) yields

$$A\sinh[k(H - h_0)] = B\sinh[k(h_0 - d)]. \tag{2.33}$$

Applying the kinematic condition (2.24) at $z = d$, to the solutions (2.15) and (2.16) (i.e, $\phi_{II}(z)$ and $\phi_{III}(z)$) we get

$$E\sinh[kd] = D\sinh[k(h_0 - d)]. \tag{2.34}$$

Further, applying the pressure continuity condition, (2.31), to the solutions (2.13) and (2.14) at $z = h_0$ gives

$$\begin{aligned} Ack\cosh[k(H - h_0)] = -ck\Bigg\{ & A\frac{k\sinh[k(H - h_0)]\cosh[kh_0 - d)]}{\sinh[k(h_0 - d)]} \\ & -E\frac{k\sinh[kd]}{\sinh[k(h_0 - d)]}\Bigg\} + A\frac{U_0\sinh[k(H - h_0)]}{h_0 - d}. \end{aligned} \tag{2.35}$$

The pressure continuity condition (2.31) applied to the solutions (2.14) and (2.15) at the interface at $z = d$ gives,

$$\begin{aligned} (U_0 - c)k\left\{A\frac{\sinh[k(H - h_0)]}{\sinh[k(h_0 - d)]} - E\frac{\sinh[kd]\cosh[k(h_0 - d)]}{\sinh[k(h_0 - d)]}\right\} + E\frac{U_0\sinh[kd]}{h_0 - d} \\ = E(U_0 - c)k\cosh[kd] - E\frac{U_0\sinh[kd]}{d}. \end{aligned} \tag{2.36}$$

The equations (2.33), (2.34), (2.35) and (2.36) can be combined to form two equations in terms of just two of the coefficients, E and A, given by

$$A\left[ck\sinh[k(H-d)]-\frac{U_0}{h_0-d}\sinh[k(H-h_0)]\sinh[k(h_0-d)]\right] \qquad (2.37)$$
$$-Eck\sinh[kd]=0,$$

$$E\left[(U_0-c)k\sinh[kh_0]-\frac{U_0h_0}{d(h_0-d)}\sinh[kd]\sinh[k(h_0-d)]\right]-A[(U_0-c)k\sinh[k(H-h_0)]=0. \qquad (2.38)$$

2.3 Dispersion relation

It follows from (2.37) and (2.38) that in order to have non-trivial solutions for A and E, the determinant of the coefficients must vanish, i.e.,

$$\begin{vmatrix} \left\{ck\sinh[k(H-d)] & -ck\sinh[kd] \\ -\frac{U_0}{h_0-d}\sinh[k(H-h_0)]\sinh[k(h_0-d)]\right\} & \\ (U_0-c)k\sinh[k(H-h_0)] & \left\{\frac{U_0h_0}{d(h_0-d)}\sinh[kd]\sinh[k(h_0-d)]\right. \\ & \left.-(U_0-c)k\sinh[kh_0]\right\} \end{vmatrix}=0.$$

Computing the determinant yields, after a little algebra, the quadratic for c given by,

$$c^2k^2\sinh[kH] - c\left[\frac{U_0k}{d(h_0-d)}\left\{d\sinh[k(H-h_0)]\sinh[kh_0] - h_0\sinh[k(H-d)]\sinh[kd]\right\}\right.$$

$$\left. + U_0k^2\sinh[kH]\right] - \left[\frac{U_0^2\sinh[k(H-h_0)]}{d(h_0-d)^2}\left\{h_0\sinh[k(h_0-d)]\sinh[kd] - kd(h_0-d)\sinh[kh_0]\right\}\right] = 0 \tag{2.39}$$

Equation (2.39) forms the dispersion relation for the instability problem in which we consider c as a function of U_0, k, h_0 and d, i.e., $c = c(U_0, k, h_0, d)$.

We now introduce the following nondimensionalization in order to simplify the dispersion relation:

$$\tilde{k} = kH,$$
$$\tilde{d} = \frac{d}{H},$$
$$\tilde{h}_0 = \frac{h_0}{H},$$
$$\tilde{c} = \frac{c}{\sqrt{gH}},$$

where the tildes denote non dimensional quantities.

Substituting the non-dimensional parameters into the dimensional dispersion relation, simplifying and dropping the tildes, we get the non-dimensional dispersion relation for c given by

$$c^2k^2\sinh[k]+cF\left[\frac{k}{d(h_0-d)}\left\{h_0\sinh[k(1-d)]\sinh[kd]-d\sinh[k(1-h_0)]\sinh[kh_0]\right\}\right.$$

$$\left.-k^2\sinh[k]\right]+\frac{F^2\sinh[k(1-h_0)]}{d(h_0-d)^2}\left[-h_0\sinh[k(h_0-d)]\sinh[kd]+kd(h_0-d)\sinh[kh_0]\right]=0, \tag{2.40}$$

where the Froude number, $F\equiv\dfrac{U_0}{\sqrt{gH}}$.

The above dispersion relation can be written in the form,

$$c^2+cF\alpha+F^2\beta=0, \tag{2.41}$$

where

$$\alpha\equiv\frac{k}{k^2d(h_0-d)\sinh[k]}\left[\left\{h_0\sinh[k(1-d)]\sinh[kd]-d\sinh[k(1-h_0)]\sinh[kh_0]\right\}-k^2\sinh[k]\right], \tag{2.42}$$

and

$$\beta\equiv\frac{\sinh[k(1-h_0)]}{k^2d(h_0-d)^2\sinh[k]}\left\{kd(h_0-d)\sinh[kh_0]-h_0\sinh[k(h_0-d)]\sinh[kd]\right\}. \tag{2.43}$$

2.4 Marginal Stability Boundary

One of the objectives in hydrodynamic stability theory is to determine the instability as a function of the flow and perturbation parameters. A particularly important property is to deduce the boundary in parameter space that separates instability from stability. This boundary is called the Marginal Stability

Boundary (MSB).

The roots of equation (2.41) are given by the quadratic formula,

$$c = \frac{-\alpha F \pm F\sqrt{\alpha^2 - 4\beta}}{2}.$$

We note that the discriminant

$$\Delta(k, h_0, d) \equiv \alpha^2 - 4\beta,$$

is independent of F and where α and β are given by (2.42) and (2.43), respectively.

Based on the sign of the discriminant, we can classify the regions of stability as follows:

1. $\Delta > 0$: This implies that there exists two real roots for c, in which case each eigenwave is purely sinusoidal and the flow is neutrally stable.

2. $\Delta < 0$: There exists a pair of complex conjugate roots. The eigenwave associated with the positive imaginary root will be a growing unstable wave and the flow is unstable. In stability theory, we are particularly interested in determining the range of wave numbers for which the flow is unstable.

3. $\Delta = 0$: The point where the discriminant vanishes is called the marginal stability boundary. This region separates the regions of stability and instability.

As an example of the transition to instability, in Figure 2.2, we plot Δ vs k assuming $h_0 = 0.5$ and $d = 0.25$ since we are considering a bottom intensified shear flow. From Figure 2.2 we see that in the region $2.887 \approx k_l < k < k_u \approx 6.227$, $\Delta < 0$ and therefore, the flow is unstable in this region. The points of marginal stability, i.e., the marginal stability boundaries, are at $k = k_l \approx 2.887$ and $k = k_u \approx 6.227$. Here, k_l is the low wavenumber cutoff and k_u is the high wavenumber cutoff.

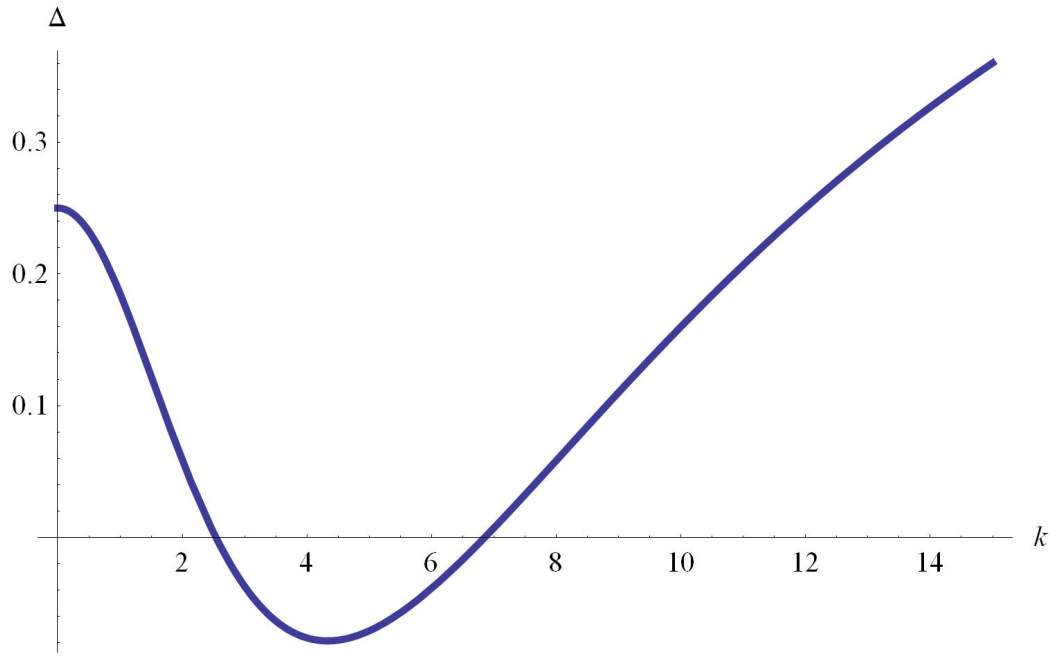

Figure 2.2: Δ vs. k for $0 \leq k \leq 15$ with $h_0 = 0.5$ and $d = 0.25$. The points of marginal stability are located at $k \approx 2.887$ and $k \approx 6.227$.

For the relevant estimate from Swaters [22], where $H \approx 800$ m, the dimensional upper wavenumber cutoff would be about 0.0077 m^{-1} and the corresponding dimensional wavelength would be about 815 m. Similarly, the dimensional low wavenumber cutoff is about 0.0036 m^{-1} and its corresponding wavelength, about 1.74 km. We note that using the estimates from Swaters [22] the Froude number, F, is calculated to be about 0.013, which indicates a subcritical flow.

The dimensional phase velocity, $c_R = \text{Re}(c)$, corresponding to the lower wavenumber, k_l is approximately 0.327 ms^{-1} and that corresponding to the high wavenumber cutoff is about 0.406 ms^{-1}.

The dimensional frequency, ω, is given by,

$$\omega = c_R k,$$

where c_R, k represent the dimensional phase velocity and wavenumber, respectively. The frequency corresponding to the low wavenumber cutoff is about

0.00253 s^{-1} and that corresponding to the upper wavenumber number cutoff is about 0.00146 s^{-1}. The period of oscillation, defined by,

$$T = \frac{2\pi}{\omega},$$

associated with the low wavenumber cutoff is found to be $T_l = 41.4$ min. and that associated with the high wavenumber cutoff is $T_u = 71.72$ min.

The graph of the frequency and the phase velocity as a function of k when $h_0 = 0.5$ and $d = 0.25$ are shown in Figures 2.3 and 2.4 respectively.

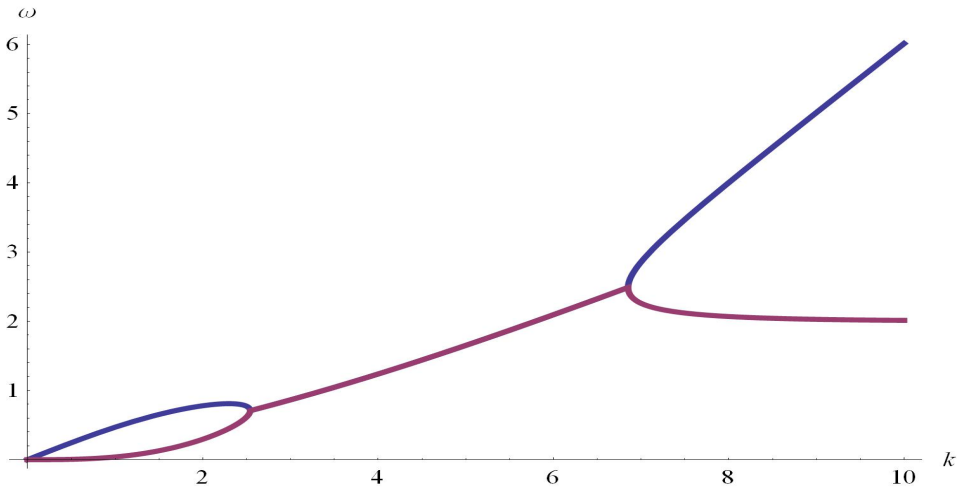

Figure 2.3: Graph of the nondimensional frequency, ωvs.k, when $h_0 = 0.5$ and $d = 0.25$.

The growth rate, σ, of the instability can be determined by,

$$\sigma = kc_I = k\,\mathrm{Im}(c), \tag{2.44}$$

where

$$c_I = -F\frac{\sqrt{-\Delta}}{2},$$

where we are assuming $\Delta \leq 0$. From Fig. 2.2, we can deduce that in the region between $k_l \approx (2.887)$ and $k_u \approx (6.227)$, $\Delta < 0$, which implies instability in that region.

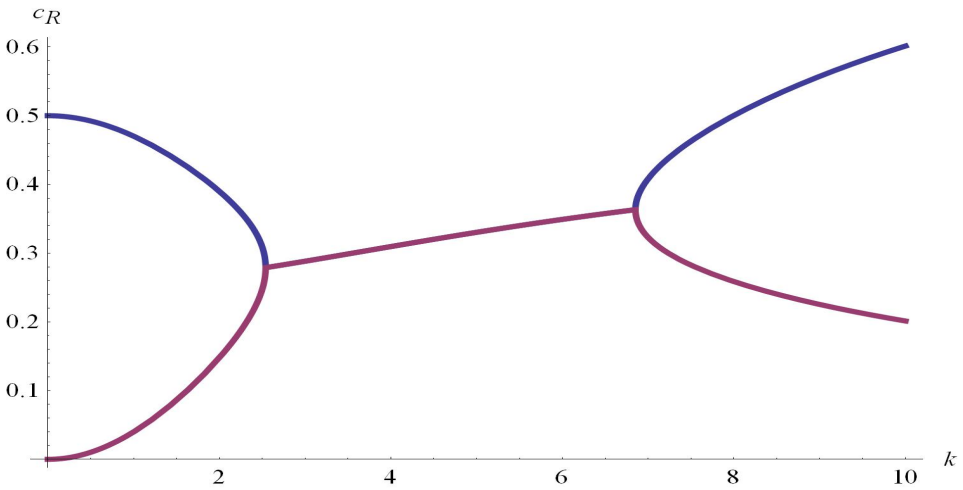

Figure 2.4: Graph of the nondimensional phase velocity, $c_R$vs.k, when $h_0 = 0.5$ and $d = 0.25$.

The dimensional growth rate is given by,

$$\sigma^\star = \frac{\sigma}{\tau},$$

where τ is the timescale, given by

$$\tau = \frac{L}{U},$$

where L has the units of length and U has the units of velocity. In our case, the timescale τ is determined to be,

$$\tau \sim \frac{H}{\sqrt{gH}} \approx 9.03s,$$

which is rapid, and $L = H \approx 800$m.

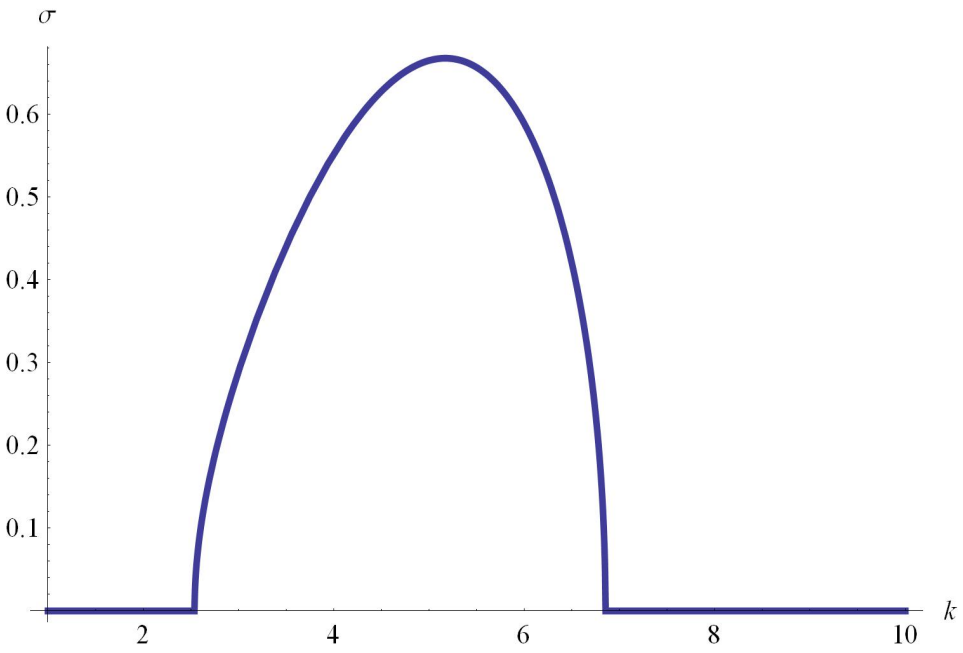

Figure 2.5: Graph of σ vs. k for $h_0 = 0.5$ and $d = 0.25$

The graph of the non dimensional growth rate, σvs.k is shown in Figure 2.5. The growth rate of the instability starts to increase at the lower wavenumber cutoff, reaches a maximum and then decreases to 0 at the upper wavenumber cutoff.

For $h_0 = 0.5$ and $d = 0.25$, the growth rate of the most unstable mode, $\sigma_{\max}$, is about 0.668 which translates to a dimensional value of 0.074 s^{-1}. This corresponds to an e-folding amplification time of 13.51 s. The e-folding amplification time is determined by

$$e_f = \frac{1}{\sigma^\star_{\max}}$$

where $\sigma^\star_{\max}$ is the dimensional growth rate of the most unstable mode.

2.5 Contour graphs

We present a series of contour plots that will describe the instability characteristics when two parameters are varied. In Figures 2.6 and 2.7 we contour plots of k_l and k_u, respectively, for the region of h_0 and d given by $0 < h_0 < 1$ and $d < h_0 < 1$ (since d is always less than h_0 from Figure 2.1).

The upper and lower wavenumber cutoffs are found by setting,

$$\Delta(k, h_0, d) = 0, \tag{2.45}$$

and solving for k as a function of h_0 and d. The solutions of equation (2.45) were obtained numerically as a function of h_0 and d. Note that d is always less than h_0 as can be deduced from the geometry of the model (Figure 2.1). The numerical solutions were obtained using the software package Mathematica.

In order to better understand the behaviour of the lower and upper wave numbers (k_l and k_u, respectively), in Figures 2.8 and 2.9, we plot k_l vs. d, and k_u vs d, respectively, for $h_0 = 0.5$. When $h_0 = 0.5$, k_l decreases to about 2 as $d \to 0.5$ with a sharp decline in k_l between $d \approx 0$ and $d \approx 0.1$. On the other hand, k_u is smaller for smaller values of d and has a 'slow' increase till $d \approx 0.4$ and a sharp incline thereafter. We similarly plot k_l and k_u for a constant $d = 0.25$ and examine their behaviour as $h_0 \to 1$. This is done in Figures 2.10 and 2.11.

When $d = 0.25$, k_l decreases monotonically as $h_0 \to 1$. However, though k_u decreases with increasing h_0 as well, the decline is not as smooth as the k_l case. The decrease in k_u is much sharper between $h_0 \approx 0$ and $h_0 \approx 0.3$, and a 'slow' decrease (to ≈ 0) thereafter. We note that this analysis is in agreement with the contour plots in Fig. 2.6.

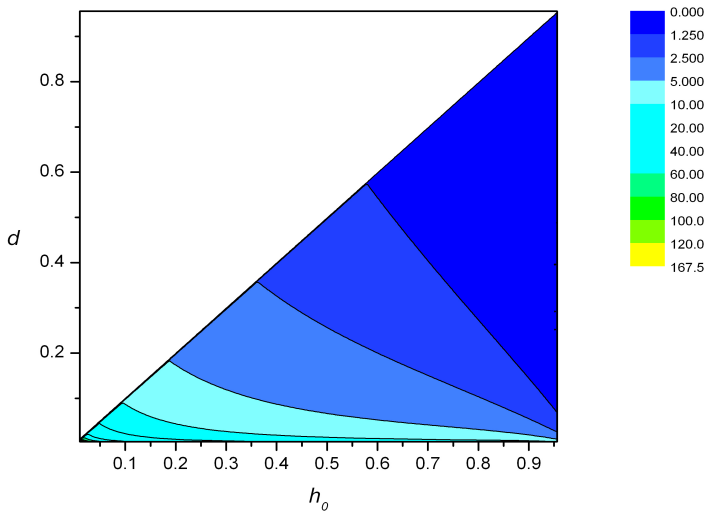

Figure 2.6: k_l contours for varying h_0 and d.

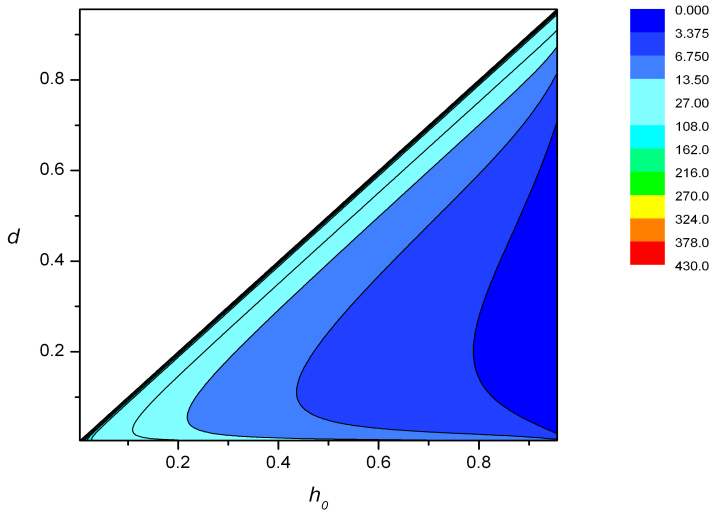

Figure 2.7: k_u contours for varying h_0 and d.

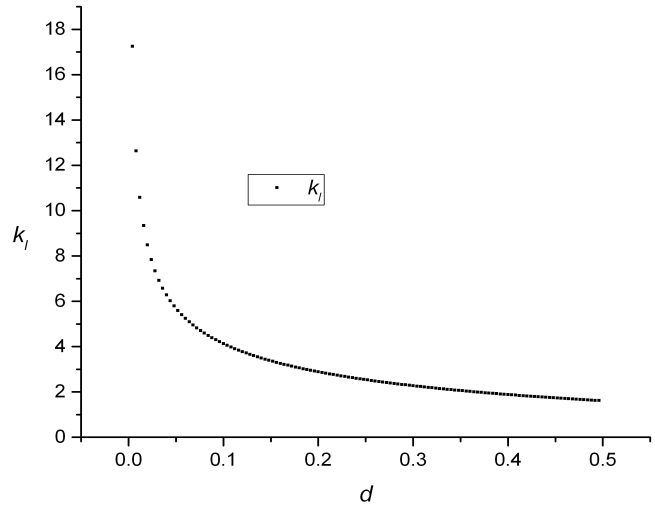

Figure 2.8: k_l for $h_0 = 0.5$ and varying d.

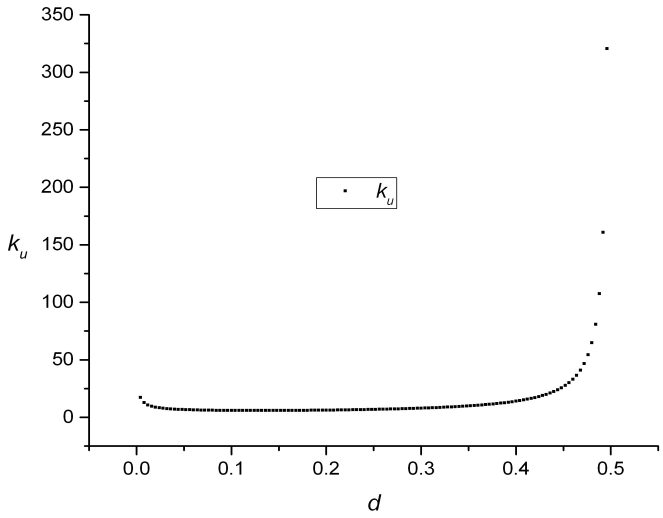

Figure 2.9: k_u for $h_0 = 0.5$ and varying d.

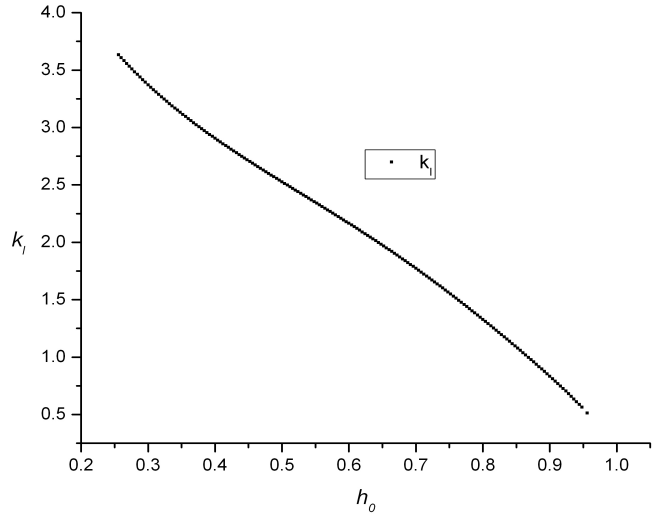

Figure 2.10: k_l contours for varying h_0 and $d = 0.25$.

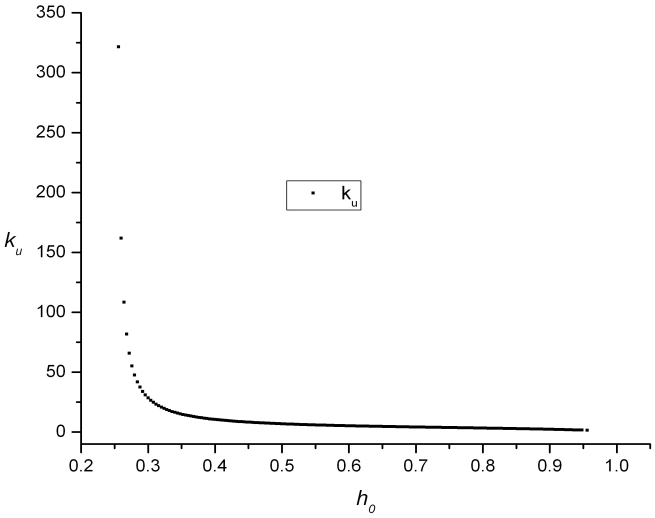

Figure 2.11: k_u contours for varying h_0 and $d = 0.25$.

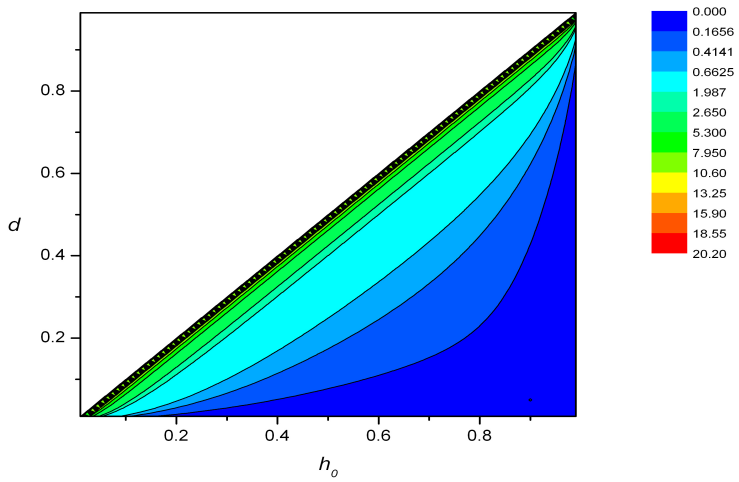

Figure 2.12: The $\sigma_{\max}$ contours for varying h_0 and d.

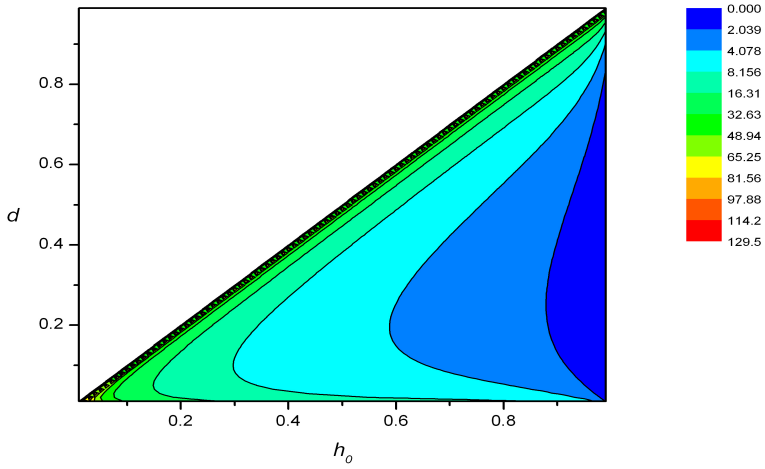

Figure 2.13: The $k_{\max}$ contours for varying h_0 and d.

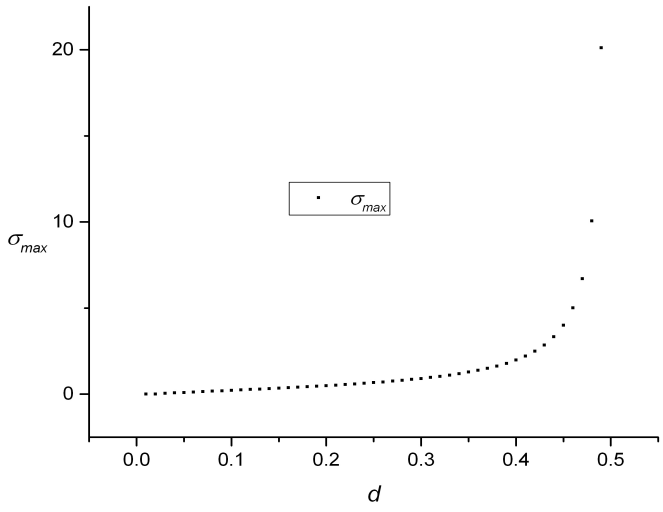

Figure 2.14: $\sigma_{\max}$, for $h_0 = 0.5$ and varying d.

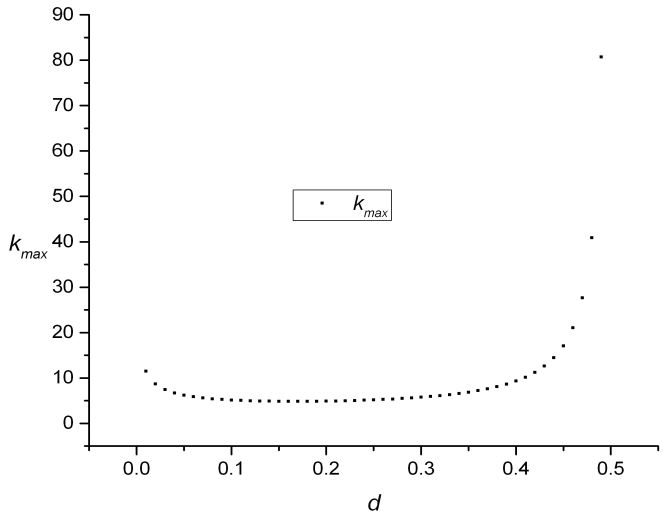

Figure 2.15: $k_{\max}$, for $h_0 = 0.5$ and varying d.

We now turn to describe how the most unstable mode varies as a function of h_0 and d. Formally, the wavenumber associated with the most unstable mode, denoted by $k_{\max}$, will satisfy

$$\frac{\partial \sigma}{\partial k}(k_{\max}) = 0 \tag{2.46}$$

for a given h_0 and d. The growth rate associated with the most unstable mode is maximum is denoted by $\sigma_{\max}$, and is given by

$$\sigma_{\max} = k_{\max}|c_I(k_{\max}, h_0, d)|.$$

Similar to our analysis of the behaviour of k_l and k_u for constant h_0 and d, we now look at the behaviour of $\sigma_{\max}$ and $k_{\max}$ for $h_0 = 0.5$. In Fig. 2.14 and 2.15, we plot $\sigma_{\max}$ and $k_{\max}$, respectively, for varying d. There is a steady increase in $\sigma_{\max}$ until the $d \approx 0.4$ point, and a sharp incline after. We notice a similar behaviour in the plot of $k_{\max}$ vs. d as well.

The determination of $k_{\max}$ and $\sigma_{\max}$ was done numerically using Mathematica. The contour plots of the growth rate ($\sigma_{\max}$) and the corresponding wavenumbers ($k_{\max}$) of the most unstable modes are shown in Fig. 2.12 and 2.13, respectively. The contours for both $\sigma_{\max}$ and $k_{\max}$, as expected, give reasonable values for $d < h_0$. However, as $d \to h_0$, both the growth rate and wave number of the most unstable mode seem to 'blow up'. These singularities are indicative of the model no longer being physical. We will examine the asymptotic structure of the dispersion relation in the next section.

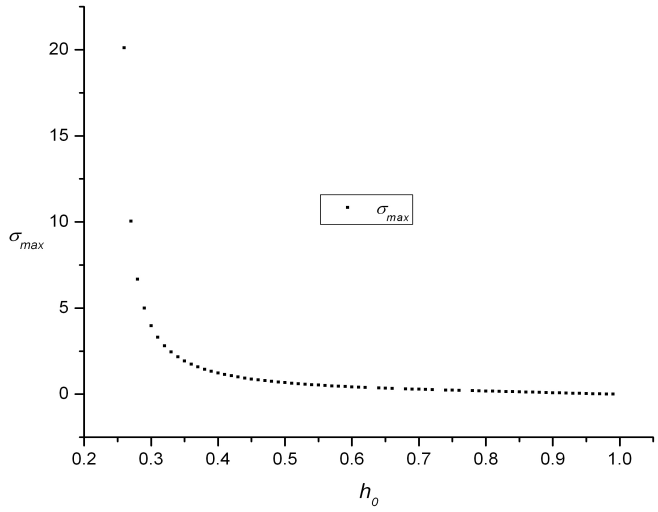

Figure 2.16: $\sigma_{\max}$ for varying h_0 and $d = 0.25$.

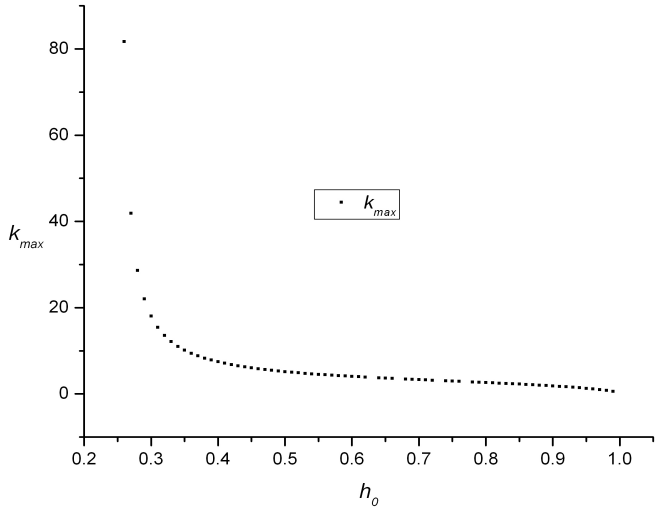

Figure 2.17: $k_{\max}$ for varying h_0 and $d = 0.25$.

In Fig. 2.16 and 2.17, we again notice a similar trend in the behaviour of $\sigma_{\max}$ and $k_{\max}$, respectively, as $h_0 \to 1$. Both, $\sigma_{\max}$ and $k_{\max}$ have a sharp decrease till $h_0 \approx 0.3$, and a steady decline to about 0 thereafter.

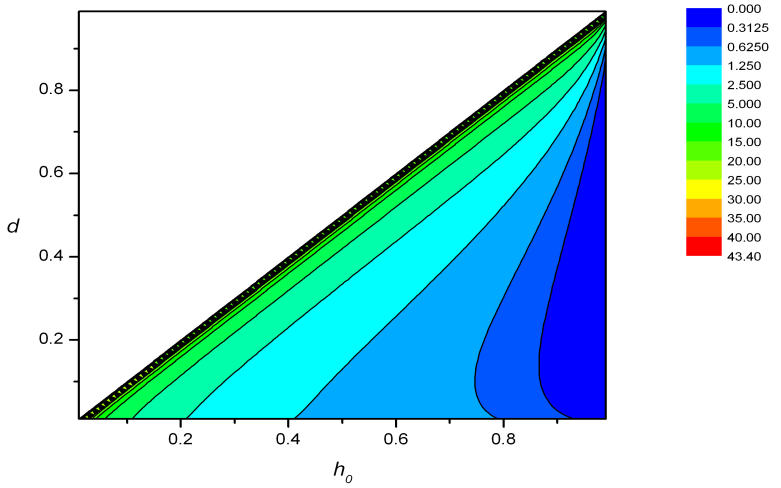

Figure 2.18: Contour plots of the frequency, ω, in the (h_0, d) plane.

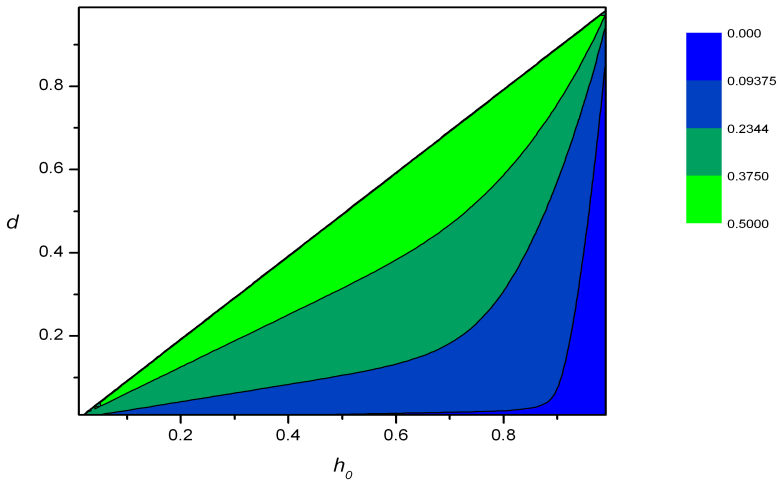

Figure 2.19: Contour plots of the phase velocity, c_R, in the (h_0, d) plane.

The frequency of the most unstable mode, denoted by $\omega_{\max}$, is given by,

$$\omega_{\max} = k_{\max} c_{R\max}, \tag{2.47}$$

where $c_{R\max}$ is given by,

$$c_{R\max} = c_R(h_0, d, k_{\max}). \tag{2.48}$$

The contours of $\omega_{\max}$, the frequency of the most unstable modes and that

of $c_R\max$, the phase velocity of the most unstable modes are shown in Fig. 2.18 and Fig. 2.19, respectively. The contours are drawn in the (h_0, d) plane.

The plots of $\omega_{\max}$ and $c_R\max$ for $h_0 = 0.5$ are shown in Fig. 2.20 and 2.21, respectively. The frequency of the most unstable mode, $\omega_{\max}$, has a steady but slow increase up to $d \approx 0.4$ and a sharp increase thereafter. The phase velocity of the most unstable mode, $c_R\max$, on the other hand is monotonically increasing as $d \to 0.5$.

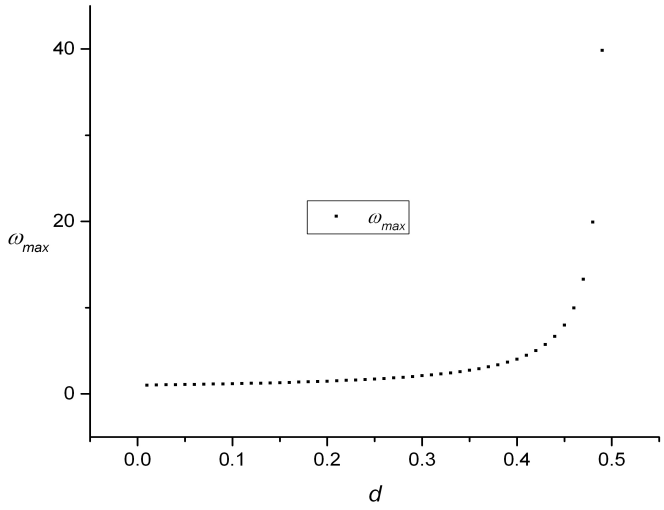

Figure 2.20: $\omega_{\max}$ for $h_0 = 0.5$ and varying d

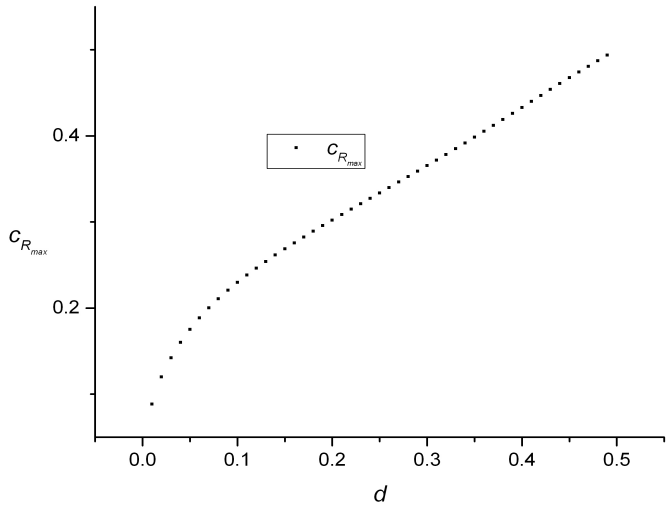

Figure 2.21: $c_{R\max}$ for $h_0 = 0.5$ and varying d

In Fig. 2.22 and Fig. 2.23, we plot $\omega_{\max}$ and $c_{\max}$, respectively, for $d = 0.25$. We notice a sharp decline in $\omega_{\max}$ for lower values of h_0 (till $h_0 \approx 0.3$), and a steady decrease to about 0 as $h_0 \to 1$. The phase velocity, $c_{\max}$, monotonically decreases as $h_0 \to 1$.

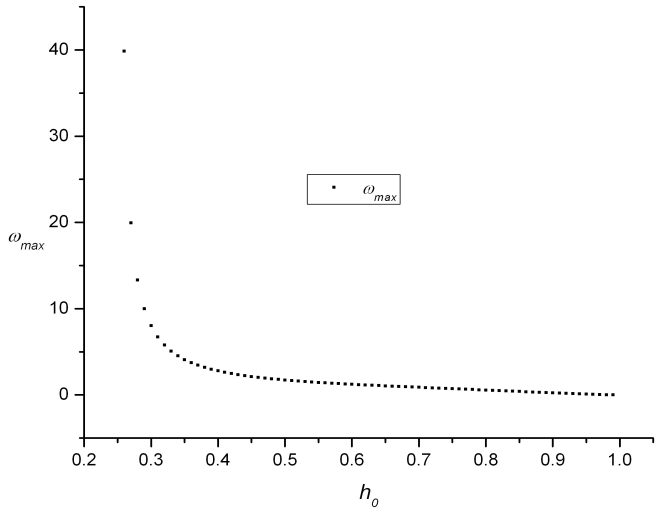

Figure 2.22: $\omega_{\max}$ for varying h_0 and $d = 0.25$

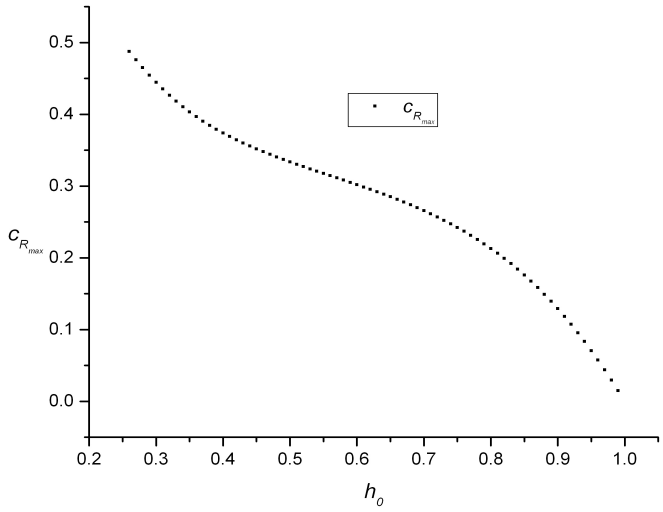

Figure 2.23: $c_{R\max}$ for varying h_0 and $d = 0.25$

2.6 Asymptotics

In this section, we determine the leading order asymptotic behaviour of the dispersion relation as $k \to 0$ and $k \to \infty$. For low values of the wavenumber ($k \to 0$), the coefficients of the dispersion relation (equation 2.41) are reduced to,

$$\alpha \sim h_0 - 1,$$

and

$$\beta \sim 0.$$

Thus, the discriminant Δ is reduced to

$$\alpha^2 - 4\beta \sim (h_0 - 1)^2 > 0,$$

which implies stability as $k \to 0$.

For large wavenumber values (k tending to ∞), we once again look at the behaviour of the coefficients of the non dimensional dispersion relation [2]

$$\alpha \sim \frac{1}{2kd} - 1,$$

and

$$\beta \sim \frac{1}{2k(h_0 - d)}.$$

Using the above approximations, the discriminant is

$$\Delta = \alpha^2 - 4\beta \sim 1 - \frac{1}{kd} - \frac{2}{k(h_0 - d)}.$$

This gives, for large values of the wavenumber, $\Delta > 0$.

Thus we conclude that $\Delta > 0$ for $k \to 0$ and hence, we have stability. When $k \to \infty$, we again have $\Delta > 0$ and stability. This is of course, to be expected, since in the region $k \to \infty$, $k > k_u$.

In this chapter, we introduced a piecewise-linear homogeneous shear flow and studied, in some detail, the stability characteristics of the same. We will follow a similar approach in Chapter 3, where we include a stable density stratification to the piecewise-linear flow profile.

Chapter 3

Stability characteristics of a shear flow in a density stratified fluid

In our quest for understanding better the shear layer instability in a nonhydrostatic fluid, we studied in the previous chapter the stability characteristics of a piecewise linear homogeneous shear flow. This chapter introduces a density stratification to the previously examined piecewise linear flow profile.

Following a similar format to Chapter 2, we begin by introducing the governing equations of the flow in Section 3.1. The matching conditions are derived in Section 3.2. We determine the dispersion relation in Section 3.3, and in 3.4 we consider some special limits of the dispersion relation. Sections 3.5 and 3.6 describe the stability characteristics from the Marginal Stability Boundary.

3.1 Governing equations

The geometry of the three-layered model we are considering is shown in Figure 3.1. The depth of the entire water column is H, η_1 and η_2 are the nondimensional disturbances in the middle and lower layer thicknesses, respectively,

compared to the scale thickness and h_0 and d are the mean layer depths for the middle and lower layers, respectively. The stratification and velocity profiles depicted in Figure 3.1 emulate real world observations of bottom intensified abyssal overflows (Swaters personal communication).

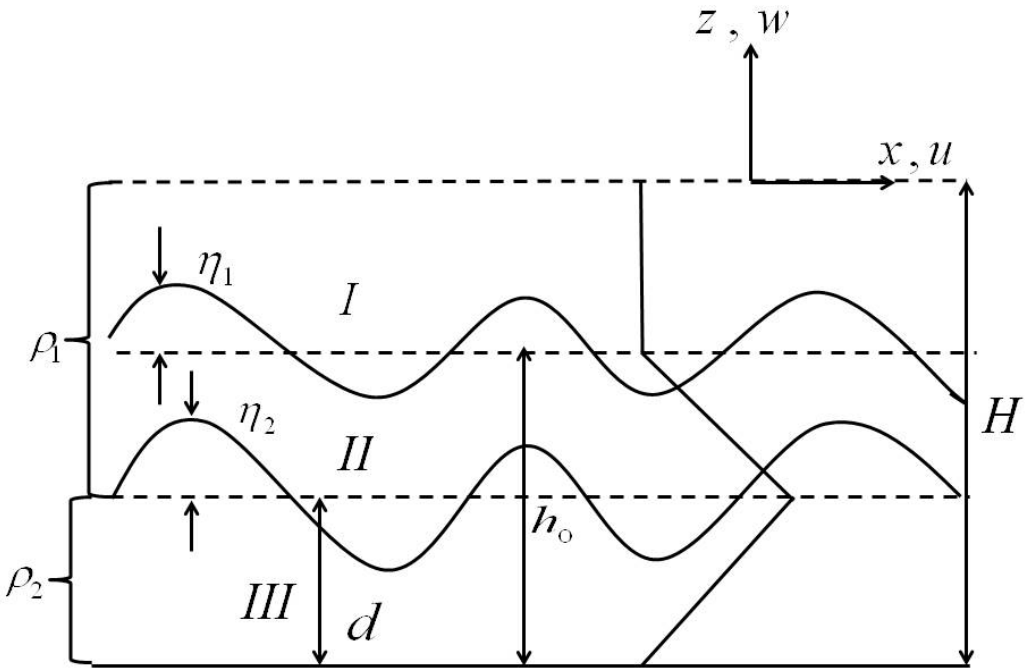

Figure 3.1: The geometry of the model

The inviscid, incompressible and stratified 2-D flow is governed by the set of partial differential equations [15]:

$$\rho(\partial_t + u\partial_x + w\partial_z)u + p_x = 0, \tag{3.1}$$

$$\rho(\partial_t + u\partial_x + w\partial_z)w + p_z = -\rho g, \tag{3.2}$$

$$(\partial_t + u\partial_x + w\partial_z)\rho = 0, \tag{3.3}$$

$$u_x + w_z = 0, \tag{3.4}$$

where u, w are the velocities in the positive x and z directions, respectively, p is the total pressure field, ρ is the density, g is acceleration due to gravity and t is the time. Equations (3.1) and (3.2) represent the conservation of horizontal and vertical momentum, respectively. Equation (3.3) represents incompressibility and equation (3.4) represents conservation of mass.

In the absence of any motion, the fluid is assumed to be in hydrostatic balance. The hydrostatic rest state is given by (3.1), (3.2) and (3.4) where $u = w = 0$, with (3.2) reducing to

$$\frac{\partial p_H}{\partial z} = -\rho_H(z)g, \tag{3.5}$$

which determines the background hydrostatic pressure field denoted by, $p_H(z)$, and given by,

$$p_H(z) = g\int_z^H \rho_H(\xi)\ d\xi, \tag{3.6}$$

where we have imposed the boundary condition, $p_H(H) = 0$, $z = H$ is the undisturbed surface of the fluid and $\rho_H(z)$ is the hydrostatic density field.

We can show that $u = U_0(z), w = 0, p = p_H(z)$ and $\rho = \rho_H(z)$ where $p_H(z)$ and ρ_H are the hydrostatic pressure and the hydrostatic density fields, respectively, is an exact steady state solution of the equations of motion for any smooth function $U_0(z)$. From the x-direction momentum equation, (3.1),

$$\rho_H(\partial_t + U_0(z)\partial_x + 0\partial_z)U_0(z) + 0 = 0,$$

which gives,

$$\rho_H \times 0 + 0 \equiv 0.$$

Substituting the exact solutions into the z-direction momentum equation, (3.2), we get

$$\rho_H(\partial_t + U_0(z)\partial_x + w\partial_z)0 + [p_H(z)]_z = \rho_H g,$$

which gives,

$$\frac{\partial p_H}{\partial z} = -\rho_H g,$$

which is satisfied on account of equation (3.5).

The exact solutions substituted into equation (3.3) gives,

$$(\partial_t + 0\partial_x + 0\partial_z)\rho_H(z) \equiv 0. \tag{3.7}$$

The mass conservation equation with the exact solutions gives,

$$[U_0]_x + 0 = 0.$$

Since U_0 is a function of z alone, the above equation is trivially satisfied. We can thus conclude that $u = U_0(z), w = 0, p = p_H(z)$ and $\rho = \rho_H(z)$ is an exact solution of the governing equations of motion.

We try to examine the linear stability of this exact solution. Thus, we now add perturbations to the exact solutions of the form

$$u(x, z, t) = U_0(z) + \tilde{u}(x, z, t), \tag{3.8}$$

$$w(x, z, t) = 0 + \tilde{w}(x, z, t), \tag{3.9}$$

$$\rho(x, z, t) = \rho_H(z) + \tilde{\rho}(x, z, t), \tag{3.10}$$

$$p(x, z, t) = p_H(z) + \tilde{p}(x, z, t), \tag{3.11}$$

where the tildes represent perturbation quantities. Substituting equations (3.8), (3.9), (3.10) and (3.11) into our model equations (3.1), (3.2), (3.3) and (3.4), neglecting nonlinear perturbation terms, dropping the tildes on the per-

turbation quantities and invoking the Boussinesq approximation, we get

$$\rho_\star(\partial_t + U_0(z)\partial_x)u + \rho_\star w U_0' = -p_x, \tag{3.12}$$

$$\rho_\star(\partial_t + U_0(z)\partial_x)w = -p_z - \rho g, \tag{3.13}$$

$$(\partial_t + U_0\partial_x)\rho + w\rho_{H_z} = 0, \tag{3.14}$$

$$u_x + w_z = 0. \tag{3.15}$$

where $\rho_\star = \dfrac{1}{H}\displaystyle\int_0^H \rho_H(z)\,dz$. Equations (3.12), (3.13), (3.14) and (3.15) are called the Linear Stability Equations and $U_0' \equiv \frac{dU_0(z)}{dz}$. Equations (3.12) and (3.13) are the perturbation momentum equations in the x and z direction respectively, (3.14) is the perturbation density equation and (3.15) is the perturbation continuity equation.

We now introduce the normal modes,

$$(u, w, \rho, p) = (u'(z), w'(z), \rho'(z), p'(z))\exp[ik(x - ct)] + \text{c.c.}, \tag{3.16}$$

where *c.c.* is the complex conjugate of the preceding term. Substituting the normal modes in the linear stability equations and dropping the primes,

$$\rho_\star(ik(U_0 - c)u + wU_0') + ikp = 0, \tag{3.17}$$

$$\rho_\star ik(U_0 - c)w + p' + \rho g = 0, \tag{3.18}$$

$$ik(U_0 - c)\rho + \rho_H' w = 0, \tag{3.19}$$

$$iku + w' = 0, \tag{3.20}$$

where $()' \equiv \frac{d()}{dz}$. Solving for u in equation (3.20), substituting it into (3.17) and using the obtained equation to eliminate p' in equation (3.18), we get

$$[\rho_\star(U_0 - c)w']' - [\rho_\star U_0' w]' - \rho_\star k^2(U_0 - c)w + ikg\rho = 0. \tag{3.21}$$

We now use equation (3.19) to eliminate ρ in equation (3.21) in the form,

$$[\rho_\star(U_0 - c)w']' - [\rho_\star U_0' w]' - \left[\frac{\rho_H' g}{U_0 - c} + \rho_\star k^2(U_0 - c)\right] w = 0. \tag{3.22}$$

Equation (3.22) is the Taylor Goldstein equation [7]. The boundary conditions are defined so that $w = 0$ at $z = H$ (i.e., a rigid-lid) and a flat bottom, $w = 0$ at $z = 0$.

Based on the continuity equation (3.15) we introduce the stream function, $\phi(x, z, t)$ such that $u = -\phi_z$ and $w = \phi_x$ [7]. We now use a normal mode of the form

$$\phi = \varphi(z)\exp[ik(x - ct)] + \text{c.c.},$$

which renders,

$$u = -\varphi', \tag{3.23}$$

and

$$w = ik\varphi. \tag{3.24}$$

Therefore, substituting (3.24) into the Taylor Goldstein equation (3.22), we get

$$[\rho_\star(U_0 - c)\varphi']' - [\rho_\star U_0'\varphi]' - \left[\frac{\rho_H' g}{U_0 - c} + \rho_\star k^2(U_0 - c)\right]\varphi = 0. \tag{3.25}$$

In this Chapter, we will assume a density profile given by,

$$\rho_H = \begin{cases} \rho_1 & d \le z \le H, \\ \rho_2 & 0 \le z \le d. \end{cases}$$

The background flow is assumed to be piecewise continuous and linear, given by,

$$U(z) = \begin{cases} 0 & h_0 \le z \le H, \\ \frac{U_0(z-h_0)}{d-h_0} & d \le z \le h_0, \\ \frac{U_0 z}{d} & 0 \le z \le d. \end{cases}$$

This profile is a model for a boundary jet located immediately adjacent to the bottom where the velocity is continuous but not differentiable and the maximum velocity is located at $z = d$ and the minimum jet velocity ($U_0(z) = 0$) is located at $z = h_0$ in the flow interior. As shown in Figure 3.1, the interval $h_0 < z < H$ will be defined as region I, $d < z < h_0$ will be defined as region II and $0 < z < d$ will be defined as region III.

Since the flow profile is linear (i.e., $U_0'' \equiv 0$, except across the interfaces), the Taylor Goldstein equation reduces to

$$\varphi'' - k^2\varphi = 0,$$

in all three regions.

We will solve the reduced TG equation in each region and then match the solutions across the interfaces where U_0' and U_0'' are not defined, both at $z = h_0$ and $z = d$, respectively, using appropriate jump conditions. The solutions for

the three regions can be written in the form,

$$\varphi_I(z) = A\sinh[k(H-z)], \tag{3.26}$$

$$\varphi_{II}(z) = B\sinh[k(z-d)] + D\sinh[k(h_0-z)], \tag{3.27}$$

and,

$$\varphi_{III}(z) = E\sinh[kz], \tag{3.28}$$

where φ_I, φ_{II} and φ_{III}, are the solutions in layers I, II and III, respectively. The boundary conditions, $\varphi = 0$ at $z = H$ (a rigid lid), and $\varphi = 0$ at $z = 0$ (non-sloping bottom) are satisfied by (3.26) and (3.28), respectively. We note that in the solutions obtained above, A, B, D and E are as yet arbitrary constants.

3.2 Matching conditions

We now impose a matching condition across the interface at $z = h_0$ where,

$$U(z) = \begin{cases} 0 & h_0 \le z \le H, \\ \frac{U_0(z-h_0)}{d-h_0} & d \le z \le h_0. \end{cases}$$

and $\rho_H = \rho_1$ for $d \le z \le H$. Another matching condition is imposed across the interface at $z = d$ where,

$$U(z) = \begin{cases} \frac{U_0(z-h_0)}{d-h_0} & d \le z \le h_0, \\ \frac{U_0 z}{d} & 0 \le z \le d. \end{cases}$$

and,

$$\rho_H = \begin{cases} \rho_1 & d \le z \le h_0, \\ \rho_2 & 0 \le z \le d. \end{cases}$$

The first condition we impose is the kinematic condition, which states that fluid particles on the interface must move with the interface without the two fluids occupying the same point at the same time and without a cavity forming between the fluids [16].

We consider the interface located at $z = h_0$ and denote u^+, w^+ as $\lim_{z\to h_0^+} u, w$, and u^-, w^- as $\lim_{z\to h_0^-} u, w$ [7]. The fully nonlinear kinematic condition is given by [7],

$$w = \phi_x = \eta_{1t} + u\eta_{1x}, \tag{3.29}$$

on $z = h_0 + \eta_1$, where η_1 is the perturbation to the location of the interface which in the background flow is located at $z = h_0$. Substituting the perturbed solutions, (3.8), (3.9) and (3.11), into the nonlinear condition (3.29), Taylor expanding about $z = h_0$ and linearizing, we get

$$w^+ = \eta_{1t} + U_0(h_0^+)\eta_{1x}, \tag{3.30}$$

at $z = h_0^+$, and

$$w^- = \eta_{1t} + U_0(h_0^-)\eta_{1x}, \tag{3.31}$$

at $z = h_0^-$.

It is now convenient to introduce normal modes of the form,

$$w = \tilde{w}(z)\exp[ik(x - ct)] + c.c., \tag{3.32}$$

$$\eta_1 = \eta_0 \exp[ik(x - ct)] + c.c., \tag{3.33}$$

where η_0 is a complex constant. Substituting the normal modes, (3.32) and (3.33) into the linearized equations (3.30) and (3.31) and dropping the tildes,

we get

$$w(h_0^+) = ik\eta_0[U_0(h_0^+) - c] \Rightarrow ik\eta_0 = \frac{w(h_0^+)}{U_0(h_0^+) - c},$$

and

$$w(h_0^-) = ik\eta_0[U_0(h_0^-) - c] \Rightarrow ik\eta_0 = \frac{w(h_0^-)}{U_0(h_0^-) - c},$$

which further implies

$$\frac{w(h_0^+)}{U_0(h_0^+) - c} = \frac{w(h_0^-)}{U_0(h_0^-) - c},$$

which can be rearranged in the form,

$$\left[\frac{w}{U_0 - c}\right] = 0, \tag{3.34}$$

on $z = h_0$, where

$$[\star] \equiv \star^+ - \star^-. \tag{3.35}$$

Equation (3.34) is the mathematical representation of the kinematic condition across the interface $z = h_0$. Since $w = ik\phi$ with the normal mode assumption and equation (3.29), the kinematic condition reduces to,

$$\left[\frac{\phi}{U_0 - c}\right] = 0.$$

Finally, since $U_0(z)$ is continuous for all z, the kinematic condition reduces to

$$[\phi] = 0, \tag{3.36}$$

at $z = h_0$. Following a procedure similar to the one above, we get the same form for the kinematic condition, (3.36) at the $z = d$ interface.

The second matching condition we need is the dynamic condition which postulates that the normal component of the stress vector at the deforming interface is continuous [16]. We first consider the condition across $z = h_0$ (where the density is continuous). For an inviscid fluid, stress continuity

implies that the total pressure across the deforming interface is continuous [7], i.e,

$$p_{ITotal}(h_0 + \eta_1) = p_{IITotal}(h_0 + \eta_1), \tag{3.37}$$

where $p_{I,II_{Total}}$ are the total pressures in layers one and two, respectively, which are given by (3.11),

$$p_{ITotal} = p_H(z) + \tilde{p}_I(x, z, t), \tag{3.38}$$

and,

$$p_{IITotal} = p_H(z) + \tilde{p}_{II}(x, z, t), \tag{3.39}$$

where $\tilde{p}_I(x, z, t)$ and $\tilde{p}_{II}(x, z, t)$ are the perturbation pressures associated with the wave field in layers one and two, respectively. From (3.37), at $z = h_0 + \eta_1$,

$$p_H(h_0 + \eta_1) + \tilde{p}_I(x, h_0 + \eta_1, t) = p_H(h_0 + \eta_1) + \tilde{p}_{II}(x, h_0 + \eta_1, t),$$

which, if Taylor expanded about $z = h_0$ and linearized, reduces to

$$\tilde{p}_I(x, h_0, t) = \tilde{p}_{II}(x, h_0, t),$$

since ρ_H is continuous across $z = h_0$ (see Figure 3.1). This gives the dynamic matching condition,

$$[p] = 0,$$

on $z = h_0$, where the tilde has been dropped.

We now introduce the normal mode assumptions,

$$p = \tilde{p}(z) \exp[ik(x - ct)] + c.c, \tag{3.40}$$

$$u = \tilde{u}\exp[ik(x-ct)] + c.c, \tag{3.41}$$

and

$$w = \tilde{w}\exp[ik(x-ct)] + c.c. \tag{3.42}$$

into the x-momentum equation, (3.12), and dropping the tildes,

$$\rho_\star\left[ik(-c)u + ikU_0(z)u\right] - \rho_\star U_0' w = -ikp. \tag{3.43}$$

Solving for p using $u = -\phi_z$ and $w = \phi_x$ gives,

$$p = (U_0 - c)\phi' - U_0'\phi,$$

so that the dynamic matching condition across $z = h_0$ will be given by,

$$[(U_0 - c)\phi' - U_0'\phi] = 0, \tag{3.44}$$

where the square brackets indicate the jump defined by (3.35).

We now derive the pressure continuity condition across $z = d$ (where the density is discontinuous). This condition is expected to be more complex since ρ_H is discontinuous across $z = d$. Following the same procedure as that for $z = h_0$, pressure continuity across the $z = d$ interface implies,

$$p_{IITotal}(d + \eta_2) = p_{IIITotal}(d + \eta_2), \tag{3.45}$$

where $p_{II,III_{Total}}$ are the total pressures in layers two and three, respectively, which are given by (3.11),

$$p_{IITotal} = p_{IIH}(z) + \tilde{p}_{II}(x, z, t),$$

and,

$$p_{IIITotal} = p_{IIIH}(z) + \tilde{p}_{III}(x, z, t),$$

where $\tilde{p}_{II}(x,z,t)$ and $\tilde{p}_{III}(x,z,t)$ are the perturbation pressures associated with the wave field in layers two and three, respectively. From (3.49), at $z = d + \eta_2$,

$$p_{IIH}(d+\eta_2) + \tilde{p}_{II}(x, d+\eta_2, t) = p_{IIIH}(d+\eta_2) + \tilde{p}_{III}(x, d+\eta_2, t),$$

which, Taylor expanded about $z = d$ reduces to,

$$-\rho_1 g\eta_2 + \tilde{p}_{II}(x,d,t) = -\rho_2 g\eta_2 + \tilde{p}_{III}(x,d,t).$$

This gives the dynamic matching condition,

$$[\rho_H g\eta_2] = [p], \tag{3.46}$$

on $z = d$, where the tilde has been dropped and $\rho_H = \rho_2 - \rho_1$.

We now introduce the normal mode assumptions,

$$p = \tilde{p}(z)\exp[ik(x-ct)] + c.c,$$

$$\eta_2 = \eta_0 exp[ik(x-ct)] + c.c,$$

$$u = \tilde{u}\exp[ik(x-ct)] + c.c,$$

and

$$w = \tilde{w}\exp[ik(x-ct)] + c.c.$$

The dynamic matching condition, (3.46), reduces to,

$$[\rho_H g\eta_0] = [p], \tag{3.47}$$

on $z = d$. Introducing the normal modes into the x-momentum equation, (3.12), and dropping the tildes, we obtain

$$\rho_\star(ik(-c)u + ikU_0(z)u) + \rho_\star U_0' w = -ikp.$$

Solving for p using $u = -\phi_z$ and $w = \phi_x$ gives,

$$p = \rho_\star((U_0 - c)\phi' - U_0'\phi). \tag{3.48}$$

We note that from the definition of (3.47), the kinematic condition, $ik\eta_0 = \dfrac{w}{U_0 - c}$, and $w = ik\phi$, the dynamic matching condition across $z = d$ will be given by,

$$\left[\rho_\star(U_0 - c)\phi' - \rho_\star U_0'\phi - \frac{\rho_H g\phi}{U_0 - c}\right] = 0, \tag{3.49}$$

where the square brackets indicate the jump defined by (3.35).

Thus applying the kinematic condition (3.36) at $z = h_0$ to the solutions (3.26) and (3.27), (i.e, $\phi_I(z)$ and $\phi_{II}(z)$) yields

$$A\sinh[k(H - h_0)] = B\sinh[k(h_0 - d)].$$

Applying the kinematic condition (3.36) at $z = d$ to the solutions (3.27) and (3.28), (i.e, $\phi_{II}(z)$ and $\phi_{III}(z)$) we get

$$D\sinh[k(h_0 - d)] = E\sinh[kd].$$

Further, applying the pressure continuity condition, (3.44), to the solutions (3.26) and (3.27) at $z = h_0$ gives

$$\begin{aligned} ckA\cosh[k(H - h_0)] = -c\left[Ak\frac{\sinh[k(H - h_0)]\cosh[k(h_0 - d)]}{\sinh[k(h_0 - d)]} - Ek\frac{\sinh[kd]}{\sinh[k(h_0 - d)]}\right] \\ +A\frac{U_0}{h_0 - d}\sinh[k(H - h_0)], \end{aligned}$$

which simplifies to,

$$A\left[ck\sinh[k(H-d)] - \frac{U_0}{h_0-d}\sinh[k(H-h_0)]\sinh[k(h_0-d)]\right]$$
$$-Eck\sinh[kd] = 0. \tag{3.50}$$

The pressure continuity condition (3.49) applied to the solutions (3.27) and (3.28) at the interface $z = d$ gives,

$$Ak(U_0-c)^2\sinh[k(H-h_0)] - E\Bigg[(U_0-c)^2k\sinh[kh_0] - g'\sinh[kd]\sinh[k(h_0-d)]$$
$$\frac{U_0(U_0-c)}{d(h_0-d)}h_0\sinh[k(h_0-d)]\sinh[kd]\Bigg] = 0, \tag{3.51}$$

where we have introduced $g' \equiv g\dfrac{\rho_2-\rho_1}{\rho_\star}$.

3.3 Dispersion relation

In order to have non-trivial solutions for A and E, the determinant of the coefficients in equations (3.50) and (3.51) must vanish:

$$\begin{vmatrix} & \left\{\dfrac{U_0(U_0-c)}{d(h_0-d)}h_0\sinh[kd]\sinh[k(h_0-d)\right. \\ k(U_0-c)^2\sinh[k(H-h_0)] & -(U_0-c)^2k\sinh[kh_0] \\ & \left.+g'\sinh[kd]\sinh[k(h_0-d)]\right\} \\ -\dfrac{U_0}{h_0-d}\sinh[k(H-h_0)]\sinh[k(h_0-d)] & -ck\sinh[kd] \\ +ck\sinh[k(H-d)] & \end{vmatrix} = 0.$$

Computing the determinant yields, after a little algebra, a cubic equation for

c given by

$$c^3k^2\sinh[kH] + c^2U_0\left[\frac{kh_0}{d(h_0-d)}\sinh[k(H-d)]\sinh[kd] - \frac{k}{h_0-d}\sinh[kh_0]\sinh[k(H-h_0)]\right.$$
$$\left.-2k^2\sinh[kH]\right] + cU_0^2\left[k^2\sinh[kH] - \frac{h_0}{d(h_0-d)^2}\sinh[kd]\sinh[k(H-h_0)]\sinh[k(h_0-d)]\right.$$
$$-\frac{kh_0}{d(h_0-d)}\sinh[kd]\sinh[k(H-d)] + \frac{2k}{h_0-d}\sinh[kh_0]\sinh[k(H-h_0)]$$
$$\left.-\frac{g'k}{U_0^2}\sinh[kd]\sinh[k(H-d)]\right] + \left[\frac{g'U_0}{h_0-d}\sinh[k(H-h_0)]\sinh[k(h_0-d)]\sinh[kd]\right.$$
$$\left.+\frac{U_0^3h_0}{d(h_0-d)^2}\sinh[kd]\sinh[k(H-h_0)]\sinh[k(h_0-d)] - \frac{U_0^3k}{h_0-d}\sinh[k(H-h_0)]\right] = 0. \tag{3.52}$$

Equation (3.52) forms the dispersion relation for the instability problems where we consider c as a function of U_0, k, h_0, d and g', i.e., $c = c(U_0, k, h_0, d, g')$.

We now introduce the following nondimensionalization in order to simplify the dispersion relation,

$$\tilde{k} = kH,$$
$$\tilde{d} = \frac{d}{H},$$
$$\tilde{h}_0 = \frac{h_0}{H},$$
$$\tilde{c} = \frac{c}{\sqrt{gH}},$$

where the tildes denote non dimensional quantities.

Substituting the non-dimensional parameters into the dimensional dispersion relation, dropping tildes and dividing by $\frac{[gH]^{3/2}}{H^2}$, we get the non-

dimensional dispersion relation

$$c^3k^2\sinh[k]+c^2F\left[\frac{kh_0}{d(h_0-d)}\sinh[k(1-d)]\sinh[kd]-2k^2\sinh[k]\right.$$
$$\left.-\frac{k}{h_0-d}\sinh[kh_0]\sinh[k(1-h_0)]\right]+c\left[F^2\left\{\frac{2k}{h_0-d}\sinh[kh_0]\sinh[k(1-h_0)]\right.\right.$$
$$-\frac{h_0}{d(h_0-d)^2}\sinh[kd]\sinh[k(1-h_0)]\sinh[k(h_0-d)]-\frac{kh_0}{d(h_0-d)}\sinh[kd]\sinh[k(1-d)]$$
$$\left.+k^2\sinh[k]\right\}-\delta k\sinh[kd]\sinh[k(1-d)]\Big]+\left[F\delta\frac{1}{(h_0-d)}\sinh[k(1-h_0)]\sinh[k(h_0-d)]\sinh[kd]\right.$$
$$\left.+F^3\sinh[k(1-h_0)]\left\{\frac{h_0}{d(h_0-d)^2}\sinh[kd]\sinh[k(h_0-d)]-\frac{k}{h_0-d}\sinh[kh_0]\right\}\right]=0, \tag{3.53}$$

where the Froude number, $F\equiv\dfrac{U_0}{\sqrt{gH}}$ and $\delta\equiv\dfrac{g'}{g}$.

3.4 Special limits

We now consider some special limits applied to the non-dimensional dispersion relation (3.53).

1. $F=0$: The first limit we consider is the no mean flow limit, i.e., $U_0=0$. This essentially means the Froude number, $F\equiv\dfrac{U_0}{\sqrt{gH}}=0$. Substituting $F=0$ in (3.53) gives

$$c^3k^2\sinh[k]-c\delta k\sinh[kd]\sinh[k(1-d)]=0,$$

which reduces to

$$c=\pm\sqrt{\frac{\delta\sinh[kd]\sinh[k(1-d)]}{k\sinh[k]}}.$$

From the above formulation, the flow is stable if and only if $\rho_2>\rho_1$, i.e.,

for a stable density stratification ($\delta > 0$). The propagating waves are called internal gravity waves [15].

2. $\delta = 0$: The second limit we consider is the homogeneous limit, i.e., $\rho_1 = \rho_2$, that is $\delta = 0$. Substituting $\delta = 0$ in the non dimensional dispersion relation (3.53) yields,

$$c^3k^2\sinh[k] + c^2F\left[\frac{kh_0}{d(h_0-d)}\sinh[k(1-d)]\sinh[kd] - 2k^2\sinh[k] - \right.$$
$$\left.\frac{k}{h_0-d}\sinh[kh_0]\sinh[k(1-h_0)]\right] + cF^2\left[-\frac{h_0}{d(h_0-d)^2}\sinh[kd]\sinh[k(1-h_0)]\sinh[k(h_0-d)]\right.$$
$$\left.+k^2\sinh[k] - \frac{kh_0}{d(h_0-d)}\sinh[kd]\sinh[k(1-d)] + \frac{2k}{h_0-d}\sinh[kh_0]\sinh[k(1-h_0)]\right]$$
$$+F^3\sinh[k(1-h_0)]\left[\frac{h_0}{d(h_0-d)^2}\sinh[kd]\sinh[k(h_0-d)] - \frac{k}{h_0-d}\sinh[kh_0]\right] = 0,$$

which reduces to,

$$k^2\sinh[k]\Big[c^3 + cF^2 - 2Fc^2\Big] + \frac{kh_0}{d(h_0-d)}\sinh[k(1-d)]\sinh[kd]\Big[c^2F - cF^2\Big]$$
$$+\frac{k}{h_0-d}\sinh[kh_0]\sinh[k(1-h_0)]\Big[2cF^2 - c^2F - F^3\Big]$$
$$+\frac{h_0}{d(h_0-d)^2}\sinh[kd]\sinh[k(1-h_0)]\sinh[k(h_0-d)]\Big[F^3 - cF^2\Big] = 0. \tag{3.54}$$

We notice that $(c - F)$ can be factored out in (3.54), which further

reduces the equation to,

$$
\begin{aligned}
&c^2k^2\sinh[k] \\
&+cF\left[\frac{k}{d(h_0-d)}\Big\{h_0\sinh[k(1-d)]\sinh[kd]-d\sinh[kh_0]\sinh[k(1-h_0)]\Big\}-k^2\sinh[k]\right] \\
&+F^2\frac{\sinh k(1-h_0)}{d(h_0-d)^2}\left[kd(h_0-d)\sinh[kh_0]-h_0\sinh[kd]\sinh[k(h_0-d)]\right]=0,
\end{aligned}
\tag{3.55}
$$

which is identical to the non dimensional dispersion relation obtained in the homogeneous case (See (2.40)). We also note here that the $\delta = 0$ limit is the non dimensional version of $g' = 0$, i.e., setting $g' = 0$ in the *dimensional* dispersion relation, (3.52) reduces the equation to the dimensional dispersion relation obtained in the homogenous case.

3.5 Marginal Stability Boundary

Along the lines of Chapter 2, having obtained the non dimensional dispersion relation in the previous section, we now turn to determining the Marginal Stability Boundary (MSB). In order to do so, we first rewrite the cubic non dimensional dispersion relation (3.53) as,

$$
\begin{aligned}
&(c-F)\left[c(c-F)k^2\sinh[k]+cF\frac{kh_0}{d(h_0-d)^2}\sinh[k(1-d)]\sinh[kd]\right. \\
&\left.-F(c-F)\frac{k}{h_0-d}\sinh[kh_0]\sinh[k(1-h_0)]-F^2\frac{h_0}{d(h_0-d)^2}\sinh[kd]\sinh[k(1-h_0)]\right] \\
&+\delta\left[\frac{F}{h_0-d}\sinh[k(1-h_0)]\sinh[k(h_0-d)]\sinh[kd]-ck\sinh[k(1-d)]\sinh[kd]\right]=0,
\end{aligned}
$$

which can be written in the form,

$$
(c-F)(c^2a+cFb+F^2d)+\delta(cM+\gamma F)=0, \tag{3.56}
$$

where

$$
\begin{aligned}
a &= k^2 \sinh[k], \\
b &= \left(\frac{kh_0}{d(h_0-d)} \sinh[k(1-d)] \sinh[kd] - \frac{k}{h_0-d} \sinh[kh_0] \sinh[k(1-h_0)] \right) - k^2 \sinh[k], \\
d &= \frac{k}{h_0-d} \sinh[kh] \sinh[k(1-h_0)] - \frac{h_0}{d(h_0-d)^2} \sinh[kd] \sinh[k(1-h_0)], \\
M &= -k \sinh[k(1-d)] \sinh[kd], \\
\gamma &= \frac{1}{h_0-d} \sinh[k(1-h_0)] \sinh[k(h_0-d)] \sinh[kd].
\end{aligned}
$$

Rewriting (3.56) in the form,

$$c^3 a + c^2 F(b-a) + cF^2(d-b) - F^3 d = 0,$$

and assuming $c = \tilde{c}F$, the above equation reduces to,

$$\tilde{c}^3 a + \tilde{c}^2(b-a) + \tilde{c}\left[(d-b) + \frac{\delta M}{F^2}\right] + \left[\frac{\delta\gamma}{F^2} - d\right] = 0.$$

Following the general procedure to solve a cubic equation, we let $\tilde{c} = t - \dfrac{b-a}{a}$ to get an equation in terms of t,

$$t^3 + pt + q = 0, \tag{3.57}$$

where p and q are defined by [1],

$$
\begin{aligned}
p &= = \frac{3a[(d-b) + \frac{\delta M}{F^2}] - (b-a^2)}{3a^2}, \\
q &= \frac{2(b-a)^3 - 9a(b-a)[(d-b) + \frac{\delta M}{F^2}] + 27a^2[\frac{\delta\gamma}{F^2} - d]}{27a^3}.
\end{aligned}
$$

The roots of the cubic (3.57) will all be real (and hence the regions of stability are obtained) when,

$$\tau \equiv -\frac{q^2}{4} - \frac{p^3}{27} \geq 0, \tag{3.58}$$

where τ is a function of k, h_0, d, δ and F. Instability occurs when $\tau < 0$ and the marginal stability boundary is obtained when $\tau \equiv 0$. The parameter surface for which,

$$\tau(k, h_0, d, \delta, F) = 0,$$

is a multidimensional hyper surface in 5-dimensional space. Therefore, it is easiest to visualize the transition from stability to instability one parameter at a time.

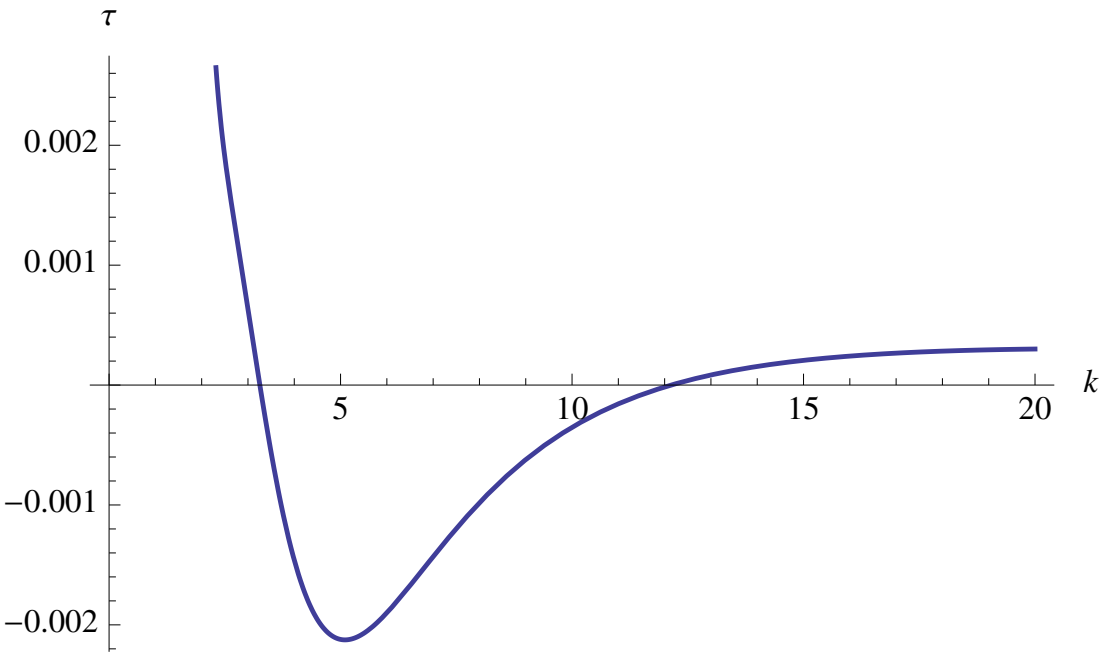

Figure 3.2: τ vs k for $0 \leq k \leq 20$ with $h_0 = 0.5, d = 0.25, \delta = 10^{-4}$ and $F = 0.013$. The points of marginal stability are located at $k \approx 3.257$ and $k \approx 12.14$.

As an example of the transition to instability, we plot in Figure (3.2) τ vs k, assuming $h_0 = 0.5, d = 0.25, F = 0.013$ and $\delta = 10^{-4}$. From Figure (3.2) we see that in the region $3.257 \approx k_l < k < k_u \approx 12.14$, $\tau < 0$ and therefore, the flow is unstable in this region. The points of marginal stability, i.e., the

marginal stability boundaries, are at $k = k_l \approx 3.257$ and $k = k_u \approx 12.14$, where k_l is the low wavenumber cutoff and k_u is the high wavenumber cutoff.

From the estimates from Swaters [22], where $H \approx 800$m, the dimensional upper wavenumber cutoff is about 0.015 m^{-1}, with the corresponding dimensional wavelength about 418.88 m. Similarly, the dimensional lower wavenumber cutoff is found to be about 0.004 m^{-1} and the corresponding dimensional wavelength about 1.57 km.

The dimensional phase velocity, $c_R = Re(c)$ corresponding to the lower wavenumber cutoff, k_l is approximately 0.0144 ms^{-1} and that corresponding to the high wavenumber cutoff, k_u is about 0.0089 ms^{-1}.

The dimensional frequency, ω, which is given by,

$$\omega = c_R k,$$

where c_R, k represent the dimensional phase velocity and wavenumber, respectively. The frequency corresponding to the low wavenumber cutoff is about 5.76×10^{-5} s^{-1} and that corresponding to the high wavenumber cutoff is approximately 1.335×10^{-4} s^{-1}.

The period of oscillation, T, given by,

$$T = \frac{2\pi}{\omega},$$

associated with the low wavenumber cutoff is $T_l = 30.3$ hours, and that corresponding to the high wavenumber cutoff is $T_u = 13$ hours.

The graphs of the frequency and the phase velocity vs. k when $h_0 = 0.5$ and $d = 0.25$ are depicted in Figures (3.3) and (3.4), respectively. In Figure (3.3), ω_1 and ω_3 coalesce when the flow is unstable, and ω_2 represents the root that is real. Similarly, in Figure (3.4), c_1 and c_2 coalesce at the region of instability, with c_2 always being 'real'.

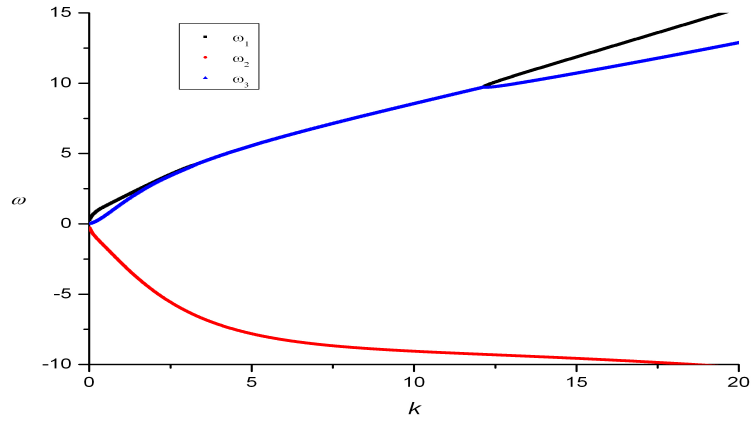

Figure 3.3: Graph of the nondimensional frequency, ω, when $h_0 = 0.5, d = 0.25, \delta = 10^{-4}$ and $F = 0.013$.

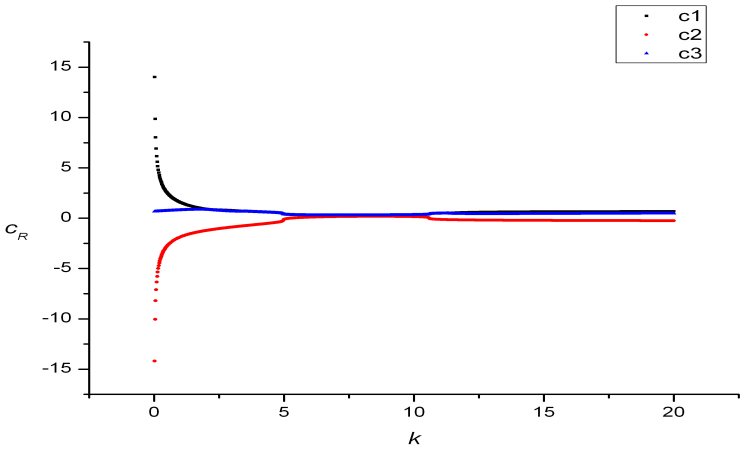

Figure 3.4: Graph of the nondimensional phase velocity, c_R, when $h_0 = 0.5, d = 0.25, \delta = 10^{-4}$ and $F = 0.013$.

The graph of the growth rate, σ, vs. k is shown in Figure (3.5). We deduce from the figure, that between the regions $k_l \approx 3.257$ and $k_u \approx 12.14$, $\tau < 0$ which implies instability in that region.

The dimensional growth rate, as determined from Chapter 2, is given by,

$$\sigma^\star = \frac{\sigma}{T},$$

where T represents the time scale (found to be 9.03 s). We note here that the usage of T, as opposed to τ as done in Chapter 2, is merely for clarity and to avoid confusion with the τ representing the stability condition in this Chapter. For $h_0 = 0.5, d = 0.25, \delta = 0.0001$ and $F = 0.013$, the growth rate of the most unstable mode, $\sigma_{\max}$ is about 0.329. This translates to a dimensional value of 0.0365 s $^{-1}$, which corresponds to an e-folding amplification time of 27.39 s.

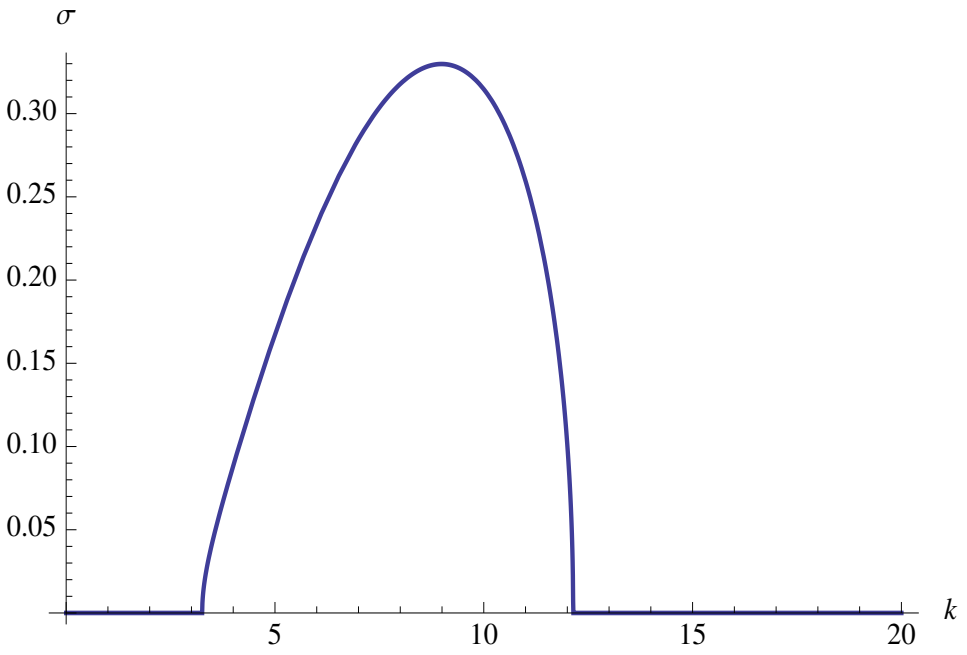

Figure 3.5: Growth rate curve for $h_0 = 0.5, d = 0.25, \delta = 10^{-4}$ and $F = 0.013$.

3.6 Contour graphs

In this section, we present a series of contour plots describing the instability characteristics when some of the parameters are varied.

Similar to Chapter 2, the upper and lower wavenumber cutoffs are determined by setting,

$$\tau(k, h_0, d, \delta, F) = 0, \tag{3.59}$$

and solving for k as a function of h_0 and d, with δ and F being constants. We first choose $\delta = 10^{-5}$ and $F = 0.013$. The solutions of (3.59) were obtained numerically using Mathematica. We note here again that d is always less than h_0 as can be deduced from the geometry of the model (3.1). The contour plots of k_l and k_u, respectively, for the region of h_0 and d given by $0 < h_0 < 1$ and $d < h_0 < 1$, are presented in Figures (3.6) and (3.7), respectively.

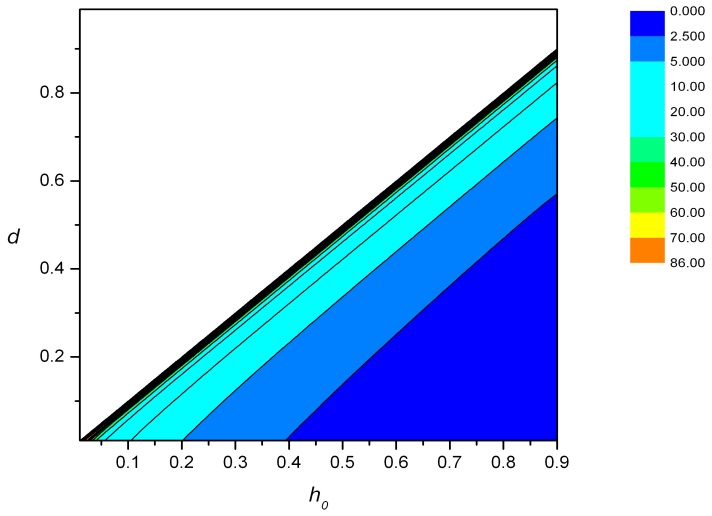

Figure 3.6: The k_l contours for varying h_0 and d with $\delta = 10^{-5}$ and $F = 0.013$.

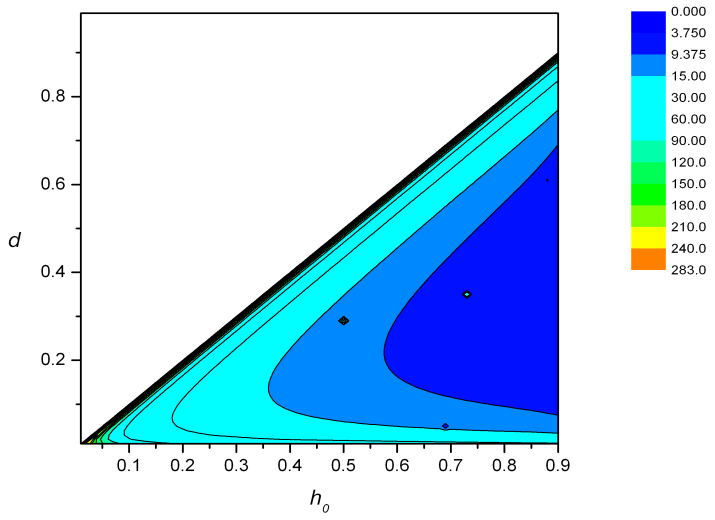

Figure 3.7: The k_u contours for varying h_0 and d with $\delta = 10^{-5}$ and $F = 0.013$.

In Figures (3.8) and (3.9) k_l and k_u as functions of h_0 and d with $\delta = 0.01$ and $F = 0.013$ are plotted, respectively.

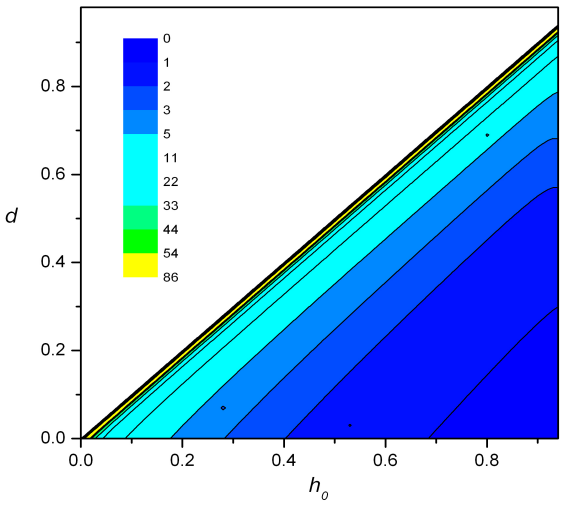

Figure 3.8: The k_l contours for varying h_0 and d with $\delta = 0.01$ and $F = 0.013$.

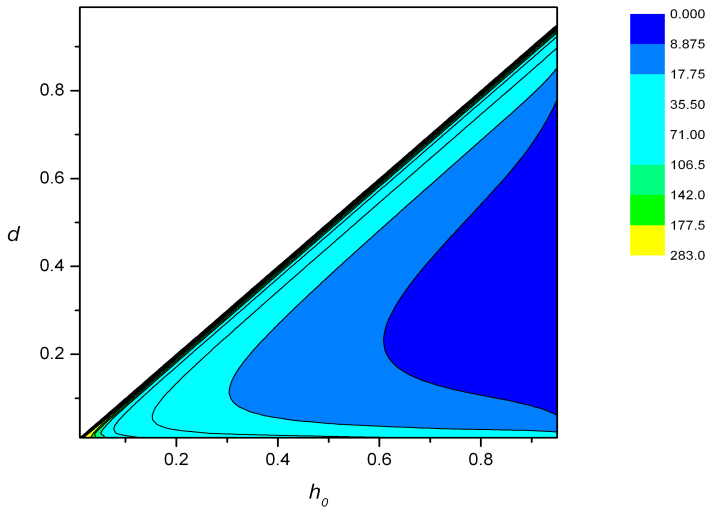

Figure 3.9: The k_u contours for varying h_0 and d with $\delta = 0.01$ and $F = 0.013$.

To better understand the behaviour of the lower and upper wave numbers, we plot k_l vs. d and k_u vs. d for $h_0 = 0.5$, $\delta = 10^{-4}$ and $F = 0.013$. Since $d < h_0$ (Figure 3.1), $d < 0.5$.

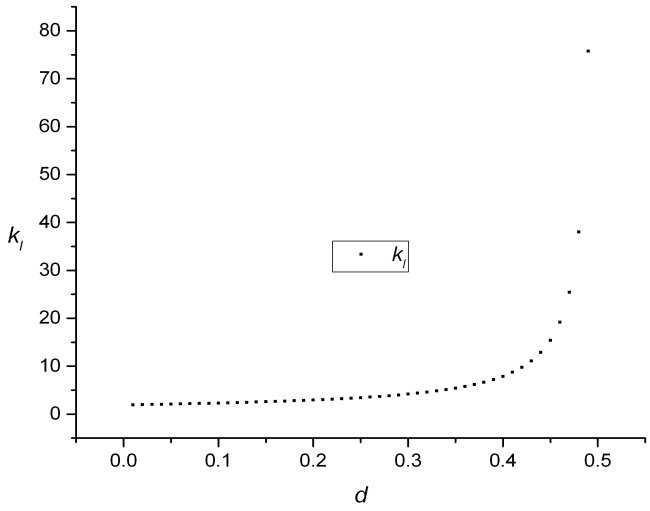

Figure 3.10: k_l for $h_0 = 0.5$ and varying d, with $\delta = 10^{-5}$ and $F = 0.013$.

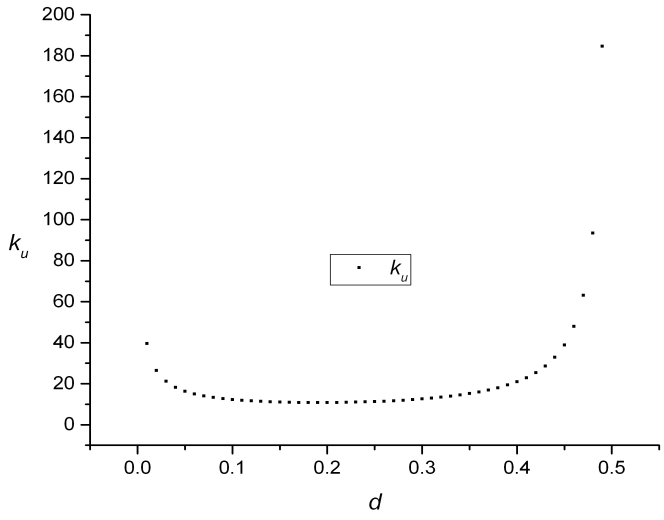

Figure 3.11: k_u for $h_0 = 0.5$ and varying d, with $\delta = 10^{-5}$ and $F = 0.013$.

From Figure 3.10, we notice the lower wavenumber k_l has a slow but steady increase until $d \approx 0.4$ and 'blows up' around $d \approx 0.5$. The upper wavenumber k_u, has an initial decrease up to $d \approx 0.05$, plateaus until $d \approx 0.4$ and has a sharp increase thereafter as $d \to 0.5$. (See Figure 3.11)

For $\delta = 10^{-5}, F = 0.013$ and $d = 0.25$, we plot k_l and k_u against h_0 in Figures 3.12 and 3.13, respectively, where $0 \leq h_0 \leq 1$. The lower wavenumber decreases for increasing h_0. Along the $d = 0.25$ contour, we notice a sharp decline in k_l around $h_0 = 0.3$, and as $h_0 \to 1$, k_l tends to 0. This can be inferred from the contour plots in Figures 3.6 and 3.7.

It is to be noted here that for $\delta = 0.01$, the numerical values of the lower and upper wave numbers have a difference in the order of about 10^{-3} from those of $\delta = 10^{-5}$. Therefore, we get very similar graphs of both, the contours (which are shown in Figures 3.8 and 3.9) and the plots of the wave numbers against one of the mean layer depths while keeping the other constant. The latter graphs have not been shown in order to avoid redundancy.

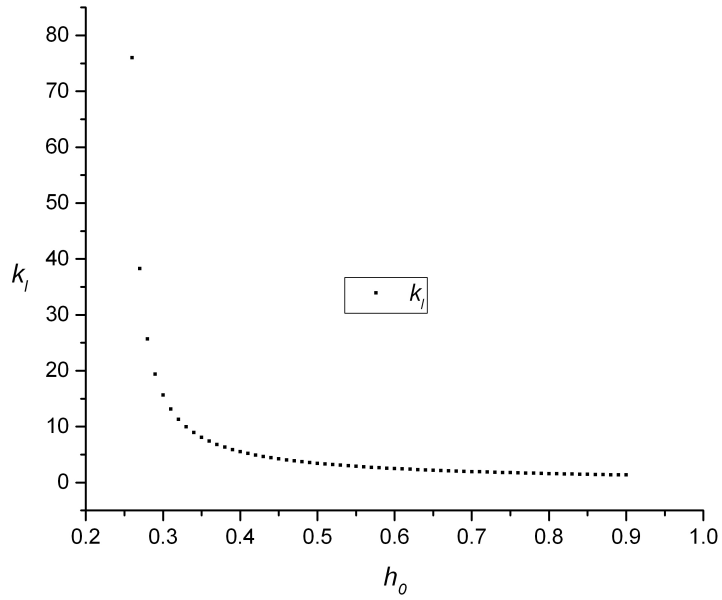

Figure 3.12: k_l for $d = 0.25$ and varying h_0, with $\delta = 10^{-5}$ and $F = 0.013$

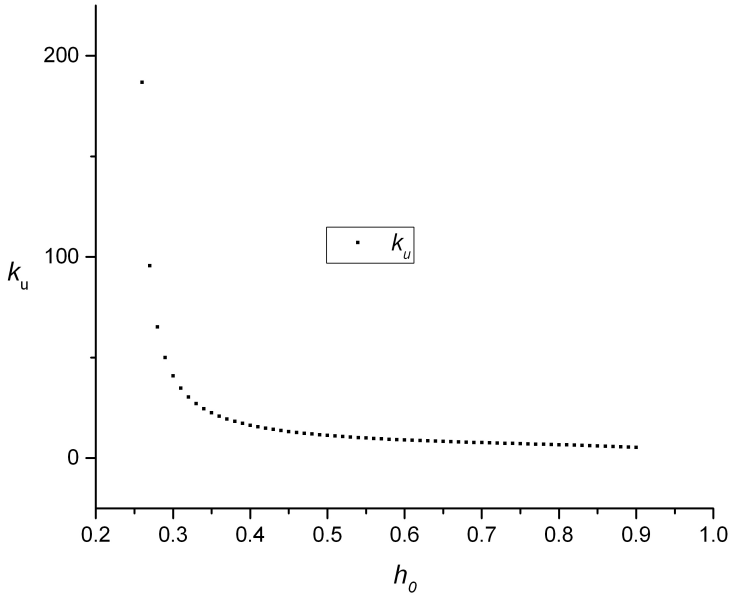

Figure 3.13: k_u for $d = 0.25$ and varying h_0, with $\delta = 10^{-5}$ and $F = 0.013$

We now turn to describe how the most unstable mode varies as a function of h_0 and d with δ and F constant. As in Chapter 2, we determine the wavenumber of the most unstable mode, $k_{\max}$, by,

$$\frac{\partial \sigma}{\partial k}(k_{\max}) = 0, \tag{3.60}$$

and the growth rate of the most unstable mode, $\sigma_{\max}$, by

$$\sigma_{\max} = k_{\max} |c_I(k_{\max}, h_0, d, \delta, F)|.$$

The determination of $k_{\max}$ and $\sigma_{\max}$ was done numerically using Mathematica. The contour plots of the growth rates($\sigma_{\max}$) of the most unstable modes and the corresponding wave numbers ($k_{\max}$) are shown in Figures (3.14) and (3.17), respectively, with $\delta = 10^{-4}$ and $F = 0.013$. The contours for both $\sigma_{\max}$ and $k_{\max}$, as expected, give reasonable values for $d < h_0$. However, as $d \to h_0$, both the growth rate and wave number of the most unstable mode seem to 'blow up', which implies that the model is no longer physical.

The growth rate of the most unstable mode for a fixed $h_0 = 0.5, \delta = 10^{-4}, F = 0.013$ and $0 \leq d < 0.5$ is depicted in Figure 3.15. Up to about $d = 0.05$, $\sigma_{\max}$ has a slow decrease, levels off until $d \approx 0.45$ and 'blows up' as $d \to 0.5$, which agrees with the contour across $h_0 = 0.5$ in Figure 3.14.

For $d = 0.25$ and $0 \leq h_0 \leq 1$, the growth rate of the most unstable mode has a sharp decrease around $h_0 = 0.3$ and decreases to 0 as $h_0 \to 1$. This is shown in Figure 3.16.

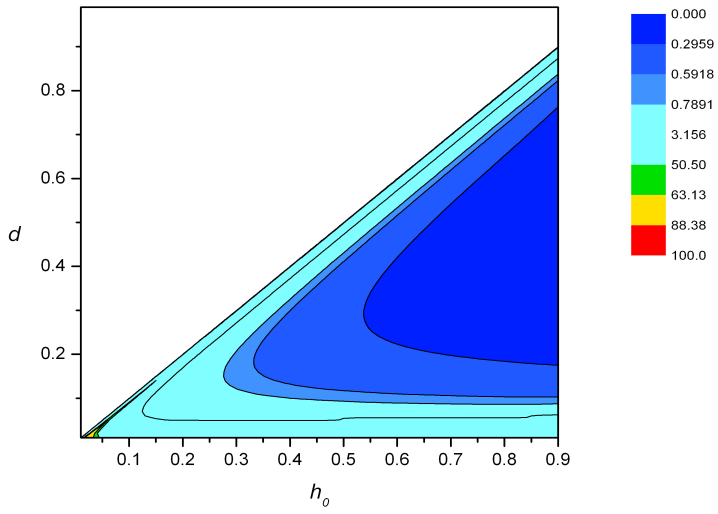

Figure 3.14: The $\sigma_{\max}$ contours for varying h_0 and d with $\delta = 10^{-4}$ and $F = 0.013$.

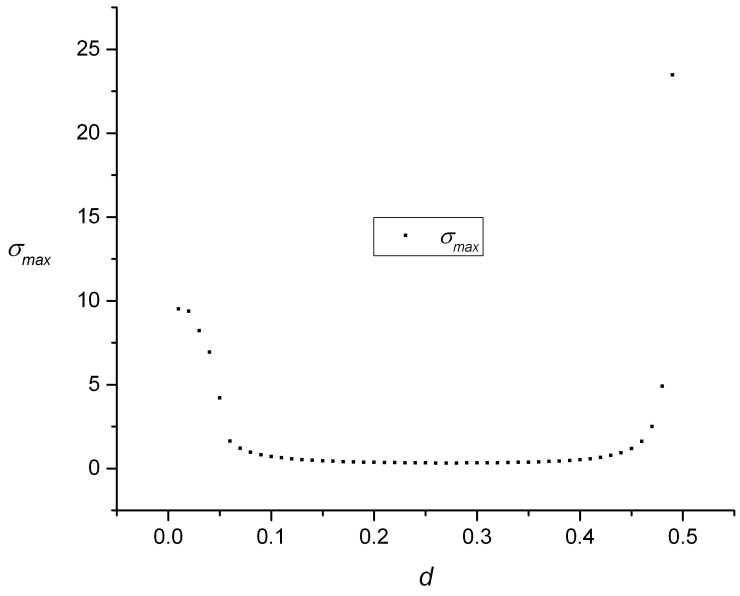

Figure 3.15: $\sigma_{\max}$ for $h_0 = 0.5$ and varying d, with $\delta = 10^{-4}$ and $F = 0.013$

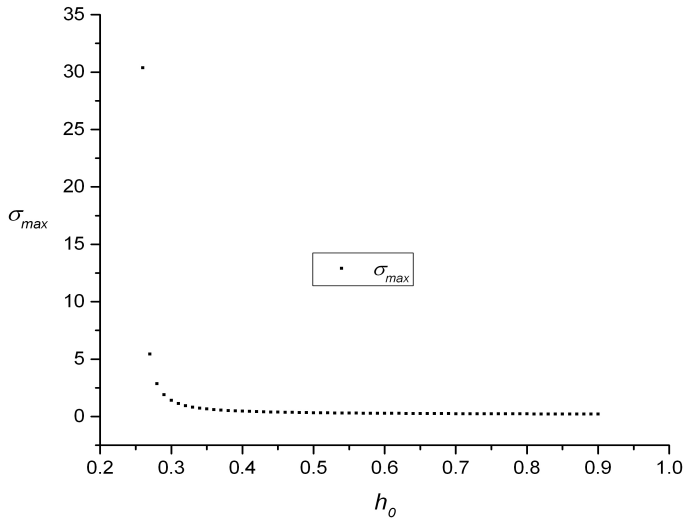

Figure 3.16: $\sigma_{\max}$ for $d = 0.25$ and varying h_0, with $\delta = 10^{-4}$ and $F = 0.013$

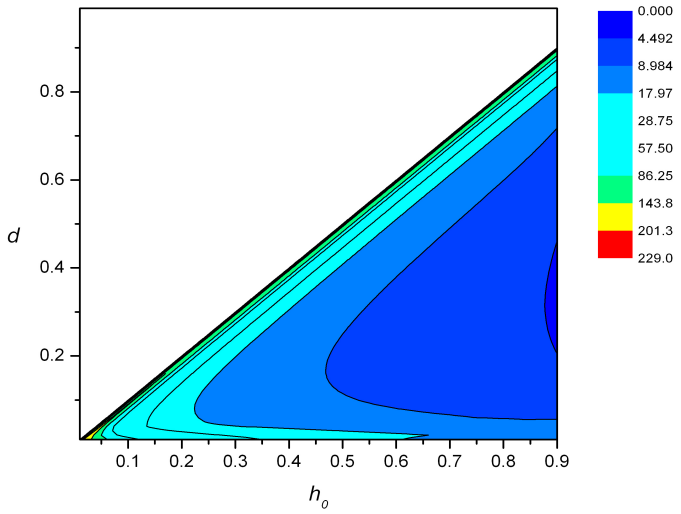

Figure 3.17: The $k_{\max}$ contours for varying h_0 and d with $\delta = 10^{-4}$ and $F = 0.013$.

The contours of the wavenumber of the most unstable mode for fixed δ and F are shown in Fig 3.17. The wavenumber of the most unstable mode when $h_0 = 0.5$, has an initial decline up to $d \approx 0.05$, enters a 'plateau' and steadily increases until about $d = 0.45$, whereupon it 'blows up' as $d \to 0.5$ (Figure 3.18)

When d is fixed at 0.25, $k_{\max}$ monotonically decreases towards 0 with increasing h_0 ($h_0 \to 1$). This is shown in Figure 3.19.

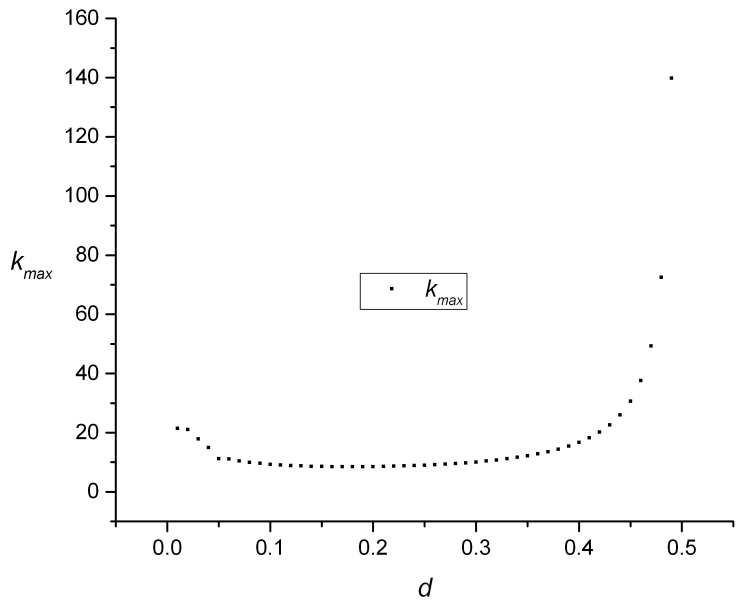

Figure 3.18: $k_{\max}$ for $h_0 = 0.5$ and varying d, with $\delta = 10^{-4}$ and $F = 0.013$

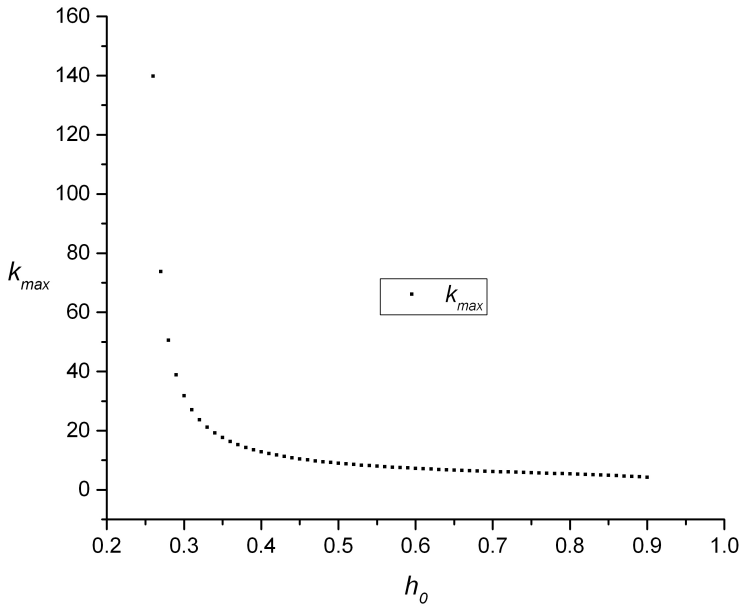

Figure 3.19: $k_{\max}$ for $d = 0.25$ and varying h_0, with $\delta = 10^{-4}$ and $F = 0.013$

The frequency of the most unstable mode, denoted by $\omega_{\max}$, is given by,

$$\omega_{\max} = k_{\max} c_{R\max}, \tag{3.61}$$

where $c_{R\max}$ is given by,

$$c_{R\max} = c_R(h_0, d, k_{\max}). \tag{3.62}$$

The contours of $\omega_{\max}$, the frequency of the most unstable modes and that of $c_{R\max}$, the phase velocity of the most unstable modes are shown in Figures (3.20) and (3.23), respectively, with $\delta = 10^{-4}$ and $F = 0.013$. The contours are drawn in the (h_0, d) plane.

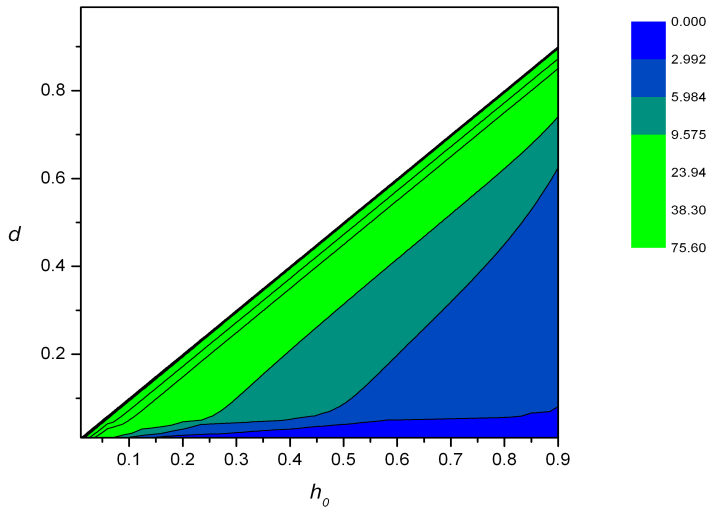

Figure 3.20: Contour plots of the frequency, ω, in the (h_0, d) plane with $\delta = 10^{-4}$ and $F = 0.013$.

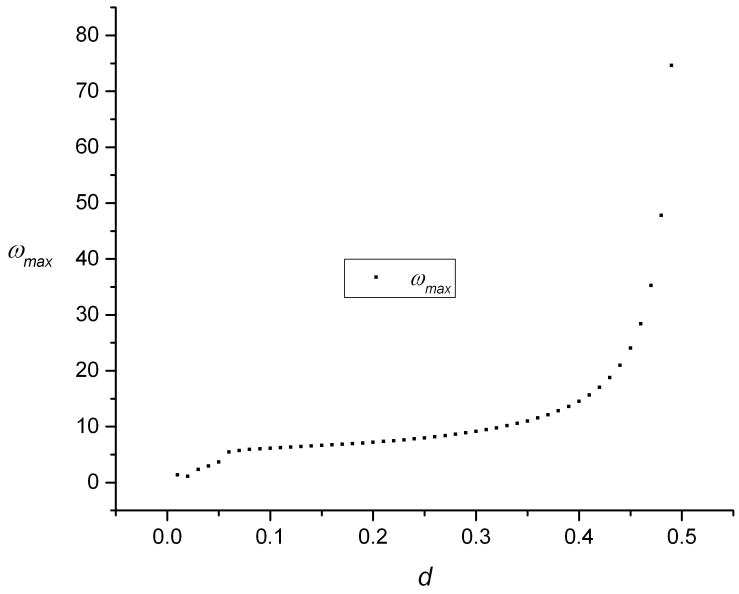

Figure 3.21: $\omega_{\max}$ for $h_0 = 0.5$ and varying d, with $\delta = 10^{-4}$ and $F = 0.013$

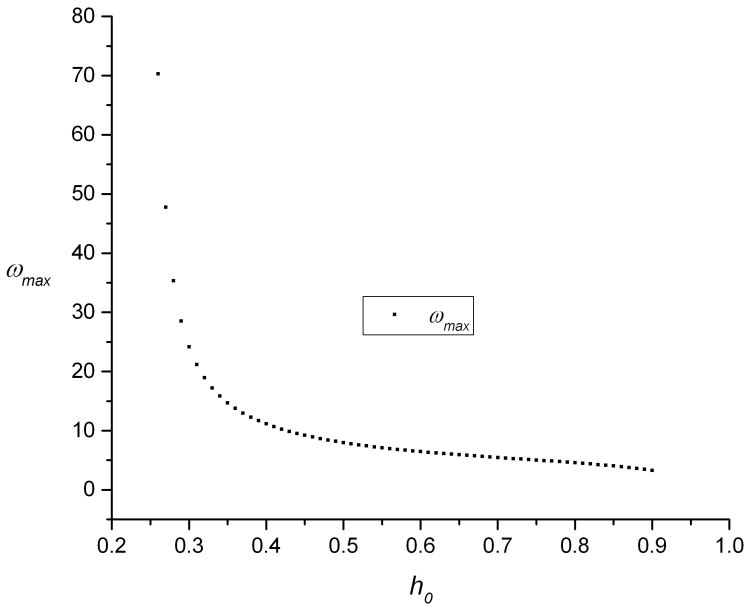

Figure 3.22: $\omega_{\max}$ for $d = 0.25$ and varying h_0, with $\delta = 10^{-4}$ and $F = 0.013$

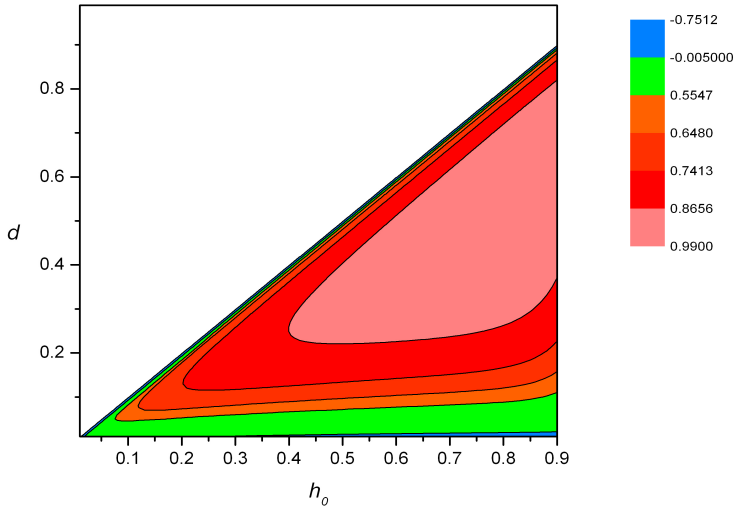

Figure 3.23: Contour plots of the phase velocity, c_R, in the (h_0, d) plane with $\delta = 10^{-4}$ and $F = 0.013$.

As before, we graph the frequency of the most unstable mode against d and h_0 in Figures 3.21 and 3.22, respectively, for $\delta = 10^{-4}$ and $F = 0.013$. For a constant h_0, $\omega_{\max}$ is monotonically increasing as $d \to 0.5$. When d is assumed constant, $\omega_{\max}$ decreases monotonically for increasing h_0.

The phase velocity of the most unstable mode, $c_{\max}$, graphed against d and h_0 for $F = 0.013$ and $\delta = 10^{-4}$ are shown in Figures 3.24 and 3.25, respectively. When $h_0 = 0.5$, $c_{\max}$ is monotonically increasing up to about $d = 0.35$ and then decreases as $d \to 0.5$. For $d = 0.25$, the phase velocity is again monotonically increasing up to $h_0 \approx 0.5$ and then decreases to $c_{\max} \approx 0.75$ as $h_0 \to 1$.

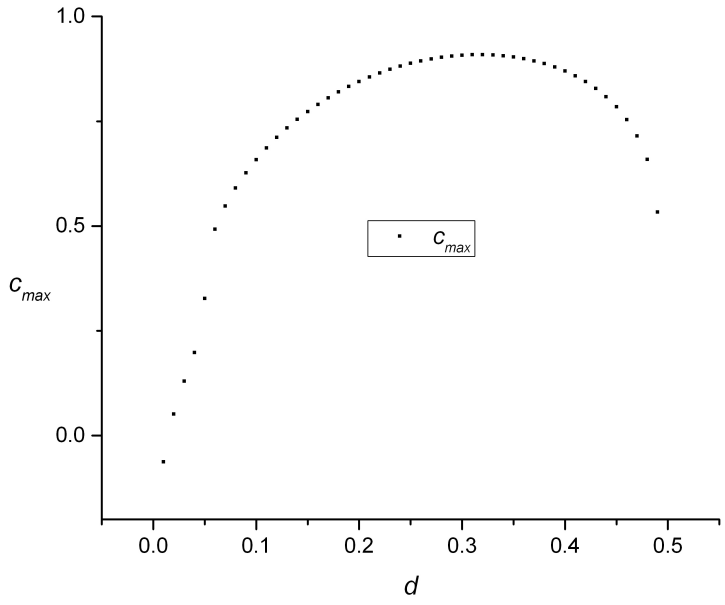

Figure 3.24: $c_{\max}$ for $h_0 = 0.5$ and varying d, with $\delta = 10^{-4}$ and $F = 0.013$

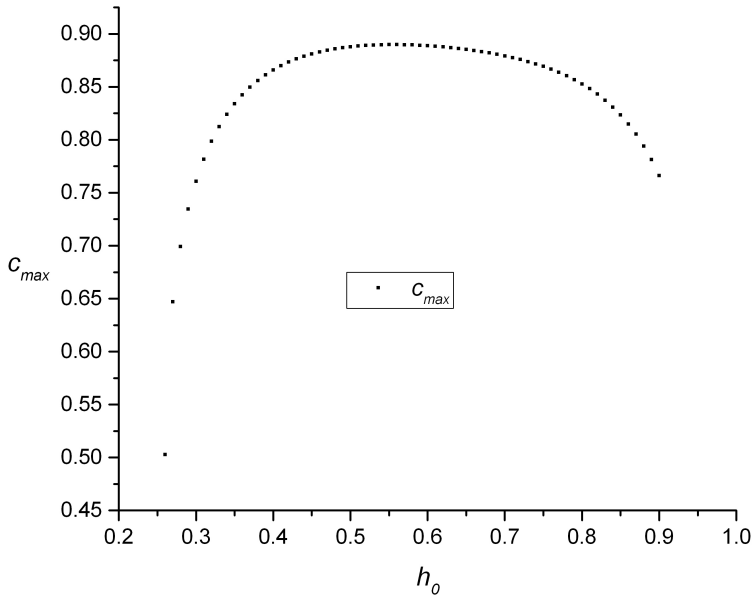

Figure 3.25: $c_{\max}$ for $d = 0.25$ and varying h_0, with $\delta = 10^{-4}$ and $F = 0.013$

In order to understand the effect of stratification on the instability of the flow, we plot the growth rate of the most unstable mode, $\sigma_{\max}$ against δ, the stratification parameter. We recall here that $\delta = \dfrac{g'}{g}$ with $g' = \dfrac{\rho_2 - \rho_1}{\rho}$ where ρ is the average density.

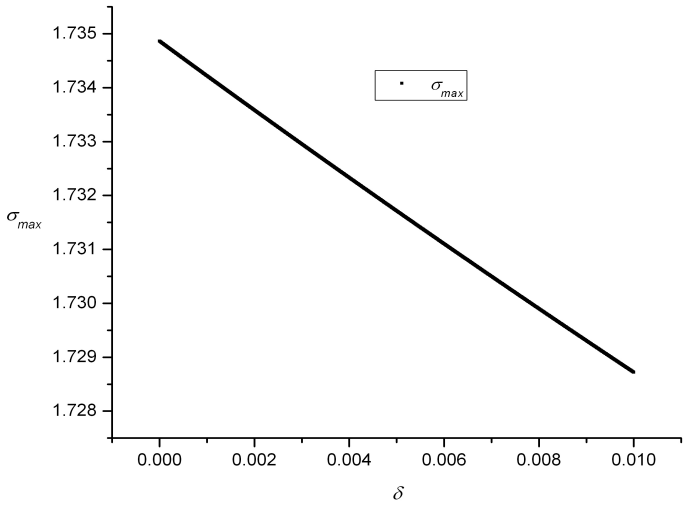

Figure 3.26: $\sigma_{\max}$ vs δ for $h_0 = 0.5, d = 0.25$ and $F = 1.5$.

In Figure (3.26) we plot $\sigma_{\max}$ vs. δ for $h_0 = 0.5, d = 0.25$ and $F = 1.5$, i.e., for a supercritical flow. The numerical computation was done using Mathematica. The x-axis representing δ goes from 10^{-4} to 10^{-2}, with increasing stratification. We notice that the growth rate of the most unstable mode decreases with increasing δ, which indicates that stratification has a stabilizing effect.

With $F = 0.013$, δ again going from 10^{-4} to 10^{-2}, $h_0 = 0.5$ and $d = 0.25$, we plot $\sigma_{\max}$ vs. δ in Figure (3.27). We note that up to $\delta \approx 0.004$, stratification has a stabilizing effect. With a stronger stratification, $\delta > 0.004$, the stratification has a destabilizing effect. This is of course, an anomaly and is counterintuitive. However, if δ is increased beyond 10^{-2}, as is done in Figure 3.28, we notice the growth rate of the most unstable mode, $\sigma_{\max}$ starts to decrease around $\delta = 0.12$, which is indicative of a stabilizing effect with increasing stratification.

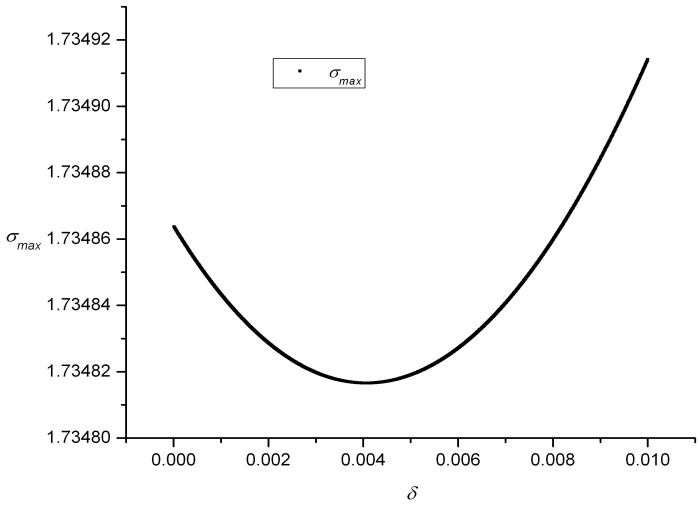

Figure 3.27: $\sigma_{\max}$ vs δ for $h_0 = 0.5, d = 0.25$ and $F = 0.013$.

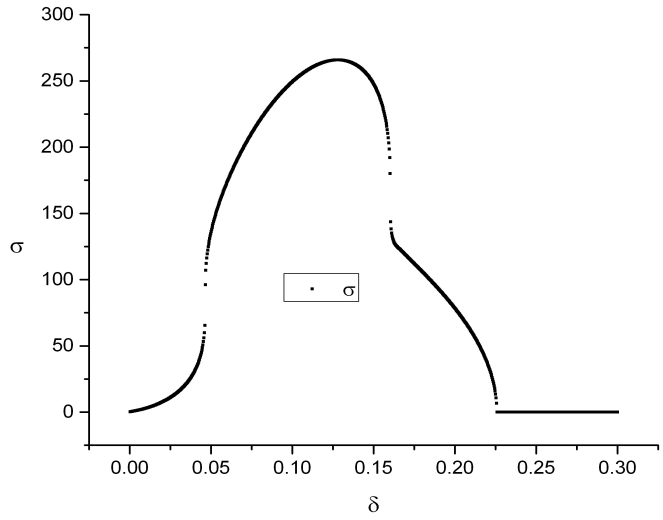

Figure 3.28: $\sigma_{\max}$ vs δ for $h_0 = 0.5, d = 0.25$ and $F = 0.013$.

Chapter 4

Conclusion

Based on the Swaters model in [22], in this thesis, we have attempted a step toward gaining a better understanding of the shear layer Kelvin-Helmholtz instability in the nonhydrostatic case. In this attempt, we initially examined in Chapter 2, a simple three-layered homogenous model with a piecewise continuous and linear flow. We used the linearized equations of motion to first derive the Rayleigh Stability Equation. To reconcile the jump across the interface with the solutions of the model equations, we then derived the matching conditions, and thereafter, used these matching conditions along with the solutions of the model equations to derive the dispersion relation. The dispersion relation in the homogenous model was found to be quadratic in c.

The marginal stability boundary, which was derived from the dispersion relation, was found to depend on the flow parameters k, h_0 and d, i.e., the wavenumber, the mean layer depth of the middle layer and the mean layer depth of the lower layer, respectively. The complexity of the dispersion relation thus derived lead us to study the transition from stability to instability one parameter at a time. Because of some singularities observed, we then examined the asymptotic structure of the dispersion relation.

For typical values for a bottom intensified shear flow, the upper wavenumber cutoff and the lower wavenumber cutoff were calculated to be 0.0077 m^{-1} and 0.0036 m^{-1}, respectively. The dimensional phase velocity, frequency, wave-

length, and the growth rate of the most unstable mode were then calculated and the e-folding amplification time was found to be 13.51 s.

Chapter 3 introduced a density stratification for the same flow profile used in Chapter 2 and a similar type of analysis was carried out. In this case, the linearized equations of motion led us to derive the Taylor-Goldstein equation. The matching conditions were then derived from the model equations. Using the matching conditions along with the solutions of the model equations, the dispersion relation was derived. The dispersion relation in this nonhomogeneous case was found to be a cubic in c.

We then obtained the marginal stability boundary, which depends on the parameters k, h_0, d, δ and F, where k, h_0 d are the same as above, and δ and F are the stratification parameter and the Froude number, respectively. The transition from instability to stability was again examined one parameter at a time. Because of the presence of stratification, we lastly examined the effects of stratification on the stability of the flow. Typical values of the bottom intensified shear flow gave us a high wavenumber cutoff and low wavenumber cutoff at 0.015 m^{-1} and 0.004 m^{-1}, respectively, and from these were calculated, the dimensional phase velocity, frequency, wavelength, and the growth rate of the most unstable mode. The e-folding amplification time was calculated to be 27.39 s.

In the course of the research done towards this thesis, we found the dispersion relation for the nonhomogeneous flow more complex than the homogeneous one for performing any sort of asymptotic analysis. A more detailed investigation of the cubic dispersion relation would possibly help explain the counterintuitive result obtained in studying the effect of stratification on the stabilization of the flow, where we had a stronger stratification leading to destabilization in the case of δ, the stratification parameter, increasing from 10^{-4} to 10^{-2}.

Introducing rotation in the model equations would be another possible next step in further examining the Kelvin-Helmholtz instability of the shear flow. In order to comply with the real world, most models employ a sloping

topography (see, for example [22], [19], [21], etc.). Therefore, investigating our problem on a sloping bottom would help us better understand the instability mechanism. Friction has also been a part of the models used in [22] and [21], so including friction in the fully nonlinear model equations would render the model more realistic. And finally, considering the limitations of linear stability theory, one could explore the solutions obtained in the weakly nonlinear case and also perhaps, the fully nonlinear equations, to obtain a more accurate picture of the transition to instability.

Bibliography

[1] Milton Abramowitz and Ireane A. Stegun. *Handbook of Mathematical Functions*. Dover Publications, 1964.

[2] Carl M. Bender and Steven A. Orszag. *Advanced Mathematical Methods for Scientists and Engineers: Asymptotic Methods and Perturbation Theory*. Springer/McGraw-Hill, 1999/1978.

[3] J. R. Carpenter, N. J. Balmforth, and G. A. Lawrence. Identifying unstable modes in stratifed shear layers. *Physics of Fluids*, 22:054104, 2010.

[4] I. P. D. DeSilva, H. J. S. Fernando, F. Eaton, and D. Hebert. Evolution of kelvin-helmholtz billows in nature and laboratory. *Earth and Planetary Science Letters*, 143:217–231, 1996.

[5] P. G. Drazin. The stability of a shear layer in an unbounded heterogeneous inviscid fluid. *Journal of Fluid Mechanics*, 4:214–224, 1958.

[6] P. G. Drazin. *Introduction to Hydrodynamic Stability*. Cambridge University Press, 2002.

[7] P. G. Drazin and W. H. Reid. *Hydrodynamic Stability*. Cambridge University Press, 1981.

[8] Robin E. Esch. The instability of a shear layer between two parallel streams. *Journal of Fluid Mechanics*, 3:289–303, 1957.

[9] Robin E. Esch. Stability of a parallel flow of a fluid over a slightly heavier fluid. *Journal of Fluid Mechanics*, 12:192–208, 1962.

[10] Philip. Hazel. Numerical studies of the stability of inviscid stratifed shear flows. *Journal of Fluid Mechanics*, 51:39–61, 1972.

[11] H. Helmholtz. On the discontinuous movements of fluids. *Edinburgh Dublin Philos. Mag. J. Sci.*, 36:337, 1868.

[12] J. Holmboe. On the behaviour of symmetric waves in stratified shear layers. *Geofysiske Publikasjoner*, 24:67–113, 1962.

[13] L. N. Howard and S. A. Maslowe. Stability of stratified shear flows. *Boundary-Layer Meteorology*, 4:511–523, 1973.

[14] W. Kelvin. Hydrokinetic solutions and observations. *Edinburgh Dublin Philos. Mag. J. Sci.*, 42:362, 1871.

[15] Pijush K. Kundu and Ira M. Cohen. *Fluid Mechanics*. Elsevier Inc., 2004.

[16] Paul H. LeBlond and Lawrence A. Mysak. *Waves in the Ocean*. Elsevier Scientific Publishing Company, 1978.

[17] Thomas P. Ray. The effects of a simple shear layer on the growth of kelvin-helmholtz instabilities. *Monthly Notices of the Royal Astronomical Society*, 198:617–625, 1982.

[18] J. W. S. Rayleigh. On the stability, or instability, of certain fluid motions. *Proceedings of the London Mathematical Society*, 12:57–72, 1880.

[19] Mateusz K. Reszka, Gordon E. Swaters, and Bruce R. Sutherland. Instability of abyssal currents in a continuously stratified ocean with bottom topography. *Journal of Physical Oceanography*, 32:3528–3550, 2002.

[20] O. Reynolds. An experimental investigation of the circumstances which determine whether the motion of water shall be direct or sinuous, and of the law of resistance in parallel channels. *Phil. Tran. Roy. Soc. Lon.*, 174:935–982, 1883.

[21] Gordon E. Swaters. Baroclinic characteristics of frictionally destabilized abyssal overflows. *Journal of Fluid Mechanics*, 489:349–379, 2003.

[22] Gordon E. Swaters. Mixed bottom-friction-kelvin-helmholtz destabilization of source-driven abyssal overflows in the ocean. *Journal of Fluid Mechanics*, 626:33–66, 2009.